

**POLITECNICO OF TURIN**

---

**Faculty of Engineering**  
Course of Biomedical Engineering

**Master Thesis**

**Electrical Characterization of Actin Filaments and  
Gold Nanoparticles Functionalized Microtubules**



**Advisor:**  
prof. Tuszynski Jacek Adam

**Candidate:**  
Serena Paladini

---

December 2022

## Acknowledgment

First and foremost, I would like to thank my supervisor, Prof. Jack Tuszynski, for his outstanding mentoring, which guided me and assisted me in achieving excellent results. Prof. Karthik Shankar and his entire team for their brilliant expertise and excellent guidance through physics problems, as well as for providing access to several devices. I would like to express my gratitude to the entire Lewis Lab team, especially Katia Simmen and Michael Staelens, who guided me through the laboratory work, and to Aarat Kalra for making good suggestions and assisting me in better understanding some biological features. My time in Edmonton was made extremely enjoyable by the cheerful and family-like atmosphere in the house where I spent 5 months, and this is all thanks to my wonderful roommates, with whom I could not have asked for better people to live with. Lucia, Marta, Stefano, Vicente, Andrea, and Juan, we adore you. Thank you for all of the laughs and good times you've given me. I'm hoping to see everyone as soon as possible.

I'd also like to thank all of the new polytechnic friends who, like me, have had this experience in Canada. Domiziano, Benedetta, Giulia, Paola, Michela, Gea, Chiara, Tommaso, Davide, Pietro, Luca, Fabiano, who have been a great support. A special thanks to Benedetta for being such a wonderful friend and for always being there for me, even on the worst of days. Thank you for inviting me to Vancouver and allowing me to experience this wonderful friendship.

And thanks to Domiziano for always believing in me, even when I didn't think I had the strength to do it on my own, and for being so close to me even 7000 kilometers away.

Finally, I'd like to thank my Italian friends. Thank you to everyone who has given me the opportunity to meet in Turin. Tommaso, Gloria, Eleonora, Cristiana, Marco, Giacomo, and Diego deserve special thanks. And I'd like to thank Giulia in particular; thank you for all of our projects together, for all of the Trapizzino, and for all of our adventures.

Thanks to all my friends from Ancona, who have supported me and have always been close to me when I needed it. I have to mention in particular Cecilia, Alessia, Silvia, Beatrice, thank you for being such sincere friends even after such a long time.

Thank you to my Erasmus friends who, even though years have passed, and our lives have taken us further apart, are still good friends to me.

Finally, I'd like to thank my family. Thanks to my sister Alice, who makes me a little more cultured every time she starts talking and who, despite the distance, is always there to give me courage and self-esteem.

And thank you to my parents; without your support over the years, I would not have had the opportunity to have had so many wonderful experiences; I owe you so much and love you.



## Abstract

Nowadays microtubules and actin filaments have aroused great interest due to their structural support abilities and their intracellular electrical signaling. Several studies have already been performed, providing experimental data on the tribological and electrical properties of these structures. The purpose of this work is to provide a better and broader characterization regarding the conductive aspect of these proteins, supplying the basis for a more precise and accurate use.

Regarding the structure of microtubules, new impedance measurements were performed by coating these structures with gold nanoparticles, metal particles that were expected to have a significant contribution to conductivity.

At the same time, we analyzed actin filaments, that together with the microtubules, constitute a significant component of the cytoskeleton, and they gained a reputation as conducting nanobiowires forming an optimized information network capable of transmitting ionic waves in cells.

For this reason, using the same techniques analysis performed on microtubules and considering the similarities between the two structural proteins, we gathered the same conductivity measurements for different concentrations of the filaments themselves, also verifying any differences between globular and polymerized actin.

The first aspect of these measurements revealed that, contrary to expectations, photodeposited nanoparticles on microtubules did not improve the ability of these proteins to conduct current; regarding the actin filaments, two relevant characteristics have been identified: the polymerized actin, arranged in filaments, has a lower impedance than its globular counterpart and, consistently with the initial hypotheses, at increasing concentrations higher conductivities correspond.

Furthermore, we worked to develop an accurate model capable of representing the properties observed from measurements of microtubules and actin filaments in solution. We hypothesized that the microtubule samples would be modeled as RC circuits, with resistive and capacitive contributions derived and analyzed. While we modeled actin filament solutions as RLC circuits, with the inductive contribution due to the ion flux flowing along the length of the characteristic helix-shaped filament.

# Contents

<b>Introduction</b> .....	<b>5</b>
<b>Chapter 1</b> .....	<b>5</b>
<b>Chapter 2</b> .....	<b>5</b>
<b>Chapter 3</b> .....	<b>5</b>
<b>Chapter 4</b> .....	<b>5</b>
<b>Chapter 5</b> .....	<b>5</b>
<b>1 Biological background</b> .....	<b>6</b>
<b>1.1 Microtubules structure</b> .....	<b>6</b>
<b>1.2 Actin structure</b> .....	<b>7</b>
<b>2 Microtubules</b> .....	<b>9</b>
<b>2.1 Exploit their features</b> .....	<b>9</b>
<b>2.2 Materials and methods</b> .....	<b>9</b>
2.2.1 Tubulin reconstitution and polymerization .....	9
2.2.2 Turbidity measurement .....	10
2.2.3 Conductivity measurement.....	11
<b>2.3 Results</b> .....	<b>12</b>
2.3.1 Turbidity measurement .....	12
2.3.2 Conductivity measurement.....	12
<b>3 Gold nanoparticles coated microtubules</b> .....	<b>15</b>
<b>3.1 Gold nanoparticles coating goals</b> .....	<b>15</b>
<b>3.2 Materials and methods</b> .....	<b>15</b>
3.2.1 Photodeposition.....	15
3.2.2 Uv-vis.....	15
3.2.3 RAMAN Spectroscopy .....	16
3.2.4 KEITHLEY Measurement .....	17
<b>3.3 Results</b> .....	<b>19</b>
3.3.1 UV-vis.....	19
3.3.2 RAMAN.....	19
3.3.3 KEITHLEY .....	20
3.3.4 Data Analysis .....	23
<b>4 Actin</b> .....	<b>28</b>
<b>4.1 Exploit Actin features</b> .....	<b>28</b>
<b>4.2 Materials and methods</b> .....	<b>29</b>
4.2.1 Actin reconstitution.....	29

4.2.2 Actin polymerization .....	30
4.2.3 Turbidity Measurement.....	30
4.2.4 KEITHLEY Measurement.....	31
<b>4.3 Results .....</b>	<b>31</b>
4.3.1 Turbidity Measurement.....	31
4.3.2 KEITHLEY.....	33
4.3.3 Data Analysis.....	35
<b>5 Conclusions .....</b>	<b>44</b>
<b>5.1 Future perspectives .....</b>	<b>45</b>
<b>Bibliography .....</b>	<b>46</b>

# Introduction

This introduction section will give an overview about different chapters and the timeline used to perform different steps:

## Chapter 1

In this chapter we will have a general view of the biological environment in which we will work, taking a closer look at the structures of microtubules and actin filaments and at the results that have been obtained over the years regarding their electro-characterization.

## Chapter 2

In this section we'll have a look into microtubules features, continuing then through the explanation of the methods used to achieve the polymerization of tubulin in MTs and the following observation of turbidity results to evaluate it and the explanation of the conductivity measurements performed on MTs solution and its buffer.

## Chapter 3

In this chapter we explain our idea to coat the microtubules, previously obtained, with gold nanoparticles, with the aim of giving to biological structure stronger conductivity features. We'll explain the processes of photodeposition that we performed in order to achieve this coating and the characterization of it through UV-vis and RAMAN spectroscopy. Finally, we measured impedance with a Keithley device to learn more about the structure's impedance frequency dependence. We'll proceed then with an accurate data analysis, comparing the experimental and the theoretical data.

## Chapter 4

In this paragraph we perform the polymerization of globular actin in actin filaments explaining the methods used and a turbidity measurement to evaluate their polymerization. Followed by impedance measurement with Keithley device, and further data analysis, that allow us to create a model of filament actin and to interpret its role in ions conductivity.

## Chapter 5

In this last chapter we summarize the most important features that our studies have highlighted and how they could be eventually used for future studies and applications.

# Chapter 1

## 1 Biological background

### 1.1 Microtubules structure

Microtubules (MTs) are cylindrical polymers composed of the heterodimers of protein  $\alpha$ ,  $\beta$ - tubulin that associate to form protofilaments running lengthwise along the microtubule wall with the  $\beta$ -tubulin subunit facing the microtubule plus end conferring a structural polarity. The  $\alpha$ - and  $\beta$ -tubulins are highly conserved. A third member of the tubulin family,  $\gamma$ -tubulin, plays a role in microtubule nucleation and assembly. Microtubule assembly is accompanied by hydrolysis of GTP associated with  $\beta$ -tubulin so that microtubules consist principally of 'GDP-tubulin' stabilized at the plus end by a short 'cap'<sup>1</sup>, Figure 1.<sup>2</sup>

The MTs outline the overall shape of cells by serving as the supports for extended morphologies such as axons, dendrites, and cilia and can be considered highly dynamic. Indeed, they can rapidly polymerize and depolymerize at their free ends. This stochastic switching between polymer growth and shrinkage is termed as "dynamic instability," and it occurs in live cells as well as in vitro with purified proteins. In cells, associated proteins that can accelerate growth, shrinkage, catastrophe, and rescue rates manipulate the microtubule network to afford active remodeling into new structures such as the mitotic spindle or to move the nucleus as a cell changes direction.<sup>3</sup>

Since the tubulin dimer possesses a high negative electric charge of  $\sim 23e$  and a large intrinsic high dipole moment of 1750 D, MTs have been implicated in electrically mediated biological aims. Indeed, they have been modelled as nanowires capable of enhancing ionic transport and simulated to receive and attenuate electrical oscillations.<sup>4</sup>

However, these biological subsystems, often do not possess the physical properties as desired for application, e.g. electric, magnetic, or optical ones, which are inherent to many inorganic materials like metals or semiconductors. Recently, the unique features of biological systems have been explored both as building blocks for bottom-up assembly or controlled deposition of novel inorganic materials and as devices with advanced structures and functionalities. Biomolecules in general reveal chemically functional surfaces with defined patterns consisting, e.g. of amino acid side chains or DNA bases that provide active sites for controlled nucleation, organization, and binding of metal particles. Motivated by future applications as nanoscaled building blocks for electronic devices, biotemplates such as, e.g. DNA strands, and biological proteins have been employed to direct the deposition of silver, palladium, platinum, or copper into conductive nanowires.<sup>5</sup>

From these studies comes our interest on trying to coat MTs with gold nanoparticles with the aim to evaluate the possible differences in conductivity using a background of BRB80, which contains within an order of magnitude of physiologically measured ionic concentrations, and BRB4, same background diluted 20 times. As subsequently reported, we found that microtubules resuspended in BRB80 decrease conductivity of the buffer, confirming expectations, while regarding the MTs in BRB4, we would have expected the microtubules to be more conductive than the background, as it has lower ionic concentration. This particular result could be explained by the role of the gold nanoparticles in our biotemplate. Moreover, we finally tried to model with an electric circuit the behavior of our solutions, characterizing them with capacitance and resistance components.

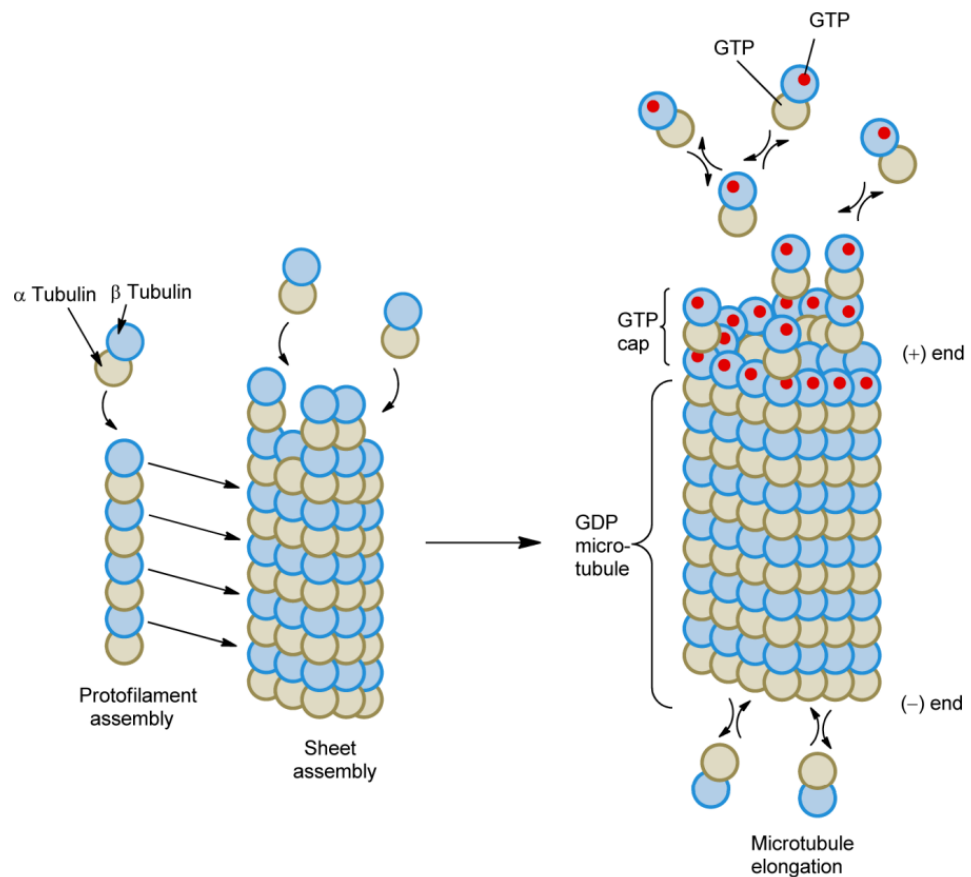


Figure 1. Focus on the protofilament forming microtubules.

## 1.2 Actin structure

Actin is one of the most abundant proteins in the cell: it represents around 5% of the total protein in eukaryotic cells and it can attain 10% in specific types of cells like muscle and microvilli-containing cells.<sup>6</sup>

It is highly conserved and participates in more protein-protein interactions than any known protein. These properties, along with its ability to transition between monomeric (G-actin) and filamentous (F-actin) states under the control of nucleotide hydrolysis, ions, and a large number of actin-binding proteins, make actin a critical player in many cellular functions, ranging from cell motility and the maintenance of cell shape and polarity to the regulation of transcription. Moreover, the interaction of filamentous actin with myosin forms the basis of muscle contraction. Owing to its central role in the cell, the actin cytoskeleton is also disrupted or taken over by numerous pathogens.<sup>7</sup>

Together with the microtubules, they constitute a significant component of the cytoskeleton, and they gained a reputation as conducting nanobiowires forming an optimized information network capable of transmitting ionic waves in cells. Functionally, actin polymers may thus be modeled as nonlinear inhomogeneous transmission lines known to propagate nonlinear dispersive solitary waves which can take form of solitons.<sup>8</sup>

However, the underlying biophysical principles and molecular mechanisms that support the ionic conductance and transport along actin filaments are still poorly understood. Approximate theories using infinitely long cylindrical filament models have become a powerful tool to characterize the electrical conductivity properties of

these polyelectrolytes. For instance, the high surface charge of the polyelectrolyte, usually present in physiological conditions, causes an inhomogeneous arrangement of counter- and co-ions forming an electrical double layer (EDL) around its surface. The accumulation of these ions builds up an ionic conductivity and capacitance layer intrinsic to the EDL.<sup>9,10</sup>

Recently, it has been introduced a multi-scale approach for infinitely long cylindrical filaments in electrolyte solutions which has been shown to capture non-trivial contributions of the diffuse part of the EDL to the ionic conductivity and capacitance.<sup>10</sup> These contributions showed a significant dependence on the EDL width, filament electric surface potential, ionic strength, and electrolyte fluid composition.<sup>11</sup> No experimental evidence has been presented to prove the ability of actin filaments to conduct electrical signals up to now, so our aim was to investigate the conditions enabling actin filaments to act as electrical transmission lines for ion flows along their lengths. Taking in consideration all these aspects, once reconstituted actin and proceeded with its polymerization, we measured the impedance of the sample solutions, comparing them with its background and with G-actin solutions. Finally, we proposed a model to characterize the actin filament properties in which each actin filament is an electric element with a capacitive, inductive, and resistive property due to its molecular structure and viscosity of the solution.

# Chapter 2

## 2 Microtubules

### 2.1 Exploit their features

MTs were historically thought to be crucial for chromosomal mobility during cell division when they were first observed in living cells in 1953. The electrical properties of MTs increasingly came into focus after studies from the 1960s and 1970s based on the successful in vitro purification of tubulin revealed that taxol had an effect on MT stabilization and that the C-terminal tails were highly acidic. Although there were hints that MTs and tubulin interacted with external electric fields in a nontrivial way, it was unclear how important their electrical characteristics were inside cells. However, when device downsizing and nanofabrication reached industrial relevance at the turn of the millennium, MTs started to get attention as prospective macromolecular transport systems. The electrostatic potential was mapped using an all-atom simulation, which also revealed the electrostatic potential difference between an MT's plus and negative ends. MTs have subsequently been demonstrated to perform significant roles, including charge storage and transit within physiologically relevant settings, both experimentally and conceptually. Their unique electrical properties have found use in sorters and direction-specific transport, while their excellent mechanical stability has led to their employment in a range of nanodevices. Molecular targets for therapy techniques based on electric fields have more recently been considered as being MTs. Their use in nanodevices outside of the cell and their functions as targets for electrically based illness treatment will certainly receive greater attention in the future.<sup>12</sup>

### 2.2 Materials and methods

#### 2.2.1 Tubulin reconstitution and polymerization

We obtained the polymerization of MTs from 1 mg of porcine brain tubulin (Cytoskeleton, Tubulin protein (>99% pure) Source: Porcine Brain Cat. # T240), prepared following the protocol of the tubulin polymerization assay, with parameters used to obtain small MTs. Briefly, we followed these steps:

First, we prepared cold GPEM buffer with 495  $\mu$ l of BRB80 (microtubule buffer solution aka PEM, 80mM PIPES, pH 6.9, 2mM  $MgCl_2$  and 0.5mM EGTA (Cytoskeleton, BST01)) and 5  $\mu$ l of GTP 100 mM, to yield a final GTP concentration of 1 mM. To allow the stabilization of the MTs we added 5  $\mu$ l of 20  $\mu$ M paclitaxel (Cytoskeleton, Taxol # TXD01) in 495  $\mu$ l GPEM, obtaining GPEM-T buffer. One lyophilized vial of unlabeled tubulin T240 stored at 4°C was finally resuspended with 400  $\mu$ l of GPEM buffer supplemented with 10% of Microtubules Cushion Buffer (glycerol) to yield 2.5mg/ml of resuspended tubulin.

MT polymerization was performed by incubating 22.7  $\mu$ M tubulin aliquots in a 37 °C water bath for 30 minutes and turbidity measurements were performed to verify the MTs polymerization.<sup>13</sup>

### 2.2.2 Turbidity measurement

Turbidity measurement can be used in this situation to prove the polymerization of MTs.

Since MTs and tubulin are significant targets for many medications, turbidity assays have been used to uncover novel compounds that are possibly effective in anti-cancer applications.

Turbidity is the most used approach for monitoring tubulin polymerization since it is simple, quantitative, and equipment-free. All that is needed is a spectrophotometer and an optically clear vessel (cuvette or multiwell plate). Quantitative measurements of assembly kinetics and steady-state polymer concentrations can be made using the turbidity data that is produced. Tubulin assembly is characterized by a lag time, a period of net increase, and a steady state (defined by a plateau). The maximum slope and plateau of the curve also grow as the amount of polymerized tubulin rises.

The three curve parameters to be examined are the lag period (the time before the OD starts to rise), the maximum rate of OD growth, and the OD at steady state.

Although there is often a strong correlation between these variables, it is not necessary.

The number of nucleation events affects the number of MTs (more nucleation events mean more MTs), but not necessarily the total amount of polymer generated, and the lag time is typically proportional to this number. A shorter lag phase might indicate more nucleation events leading to shorter MTs, even though the total mass of MTs is the same (two different curves settle to the same plateau value).<sup>14</sup>

To perform turbidity analysis, we used the SpectraMax® iD5 microplate reader (Figure 3), in 340 nm absorbance kinetic mode for 40 minutes and we quickly pipetted 100  $\mu$ l of the tubulin samples previously obtained into a 96 well plate. One point was obtained every 30 seconds for a total of 81 and before each new reading the plate was shaken. All parameters are reported in Table 1. The data were finally collected and analyzed using the Software OriginLab.



Figure 2. *SpectraMax iD5 microplate reader.*

Parameters	Settings
Measurement Mode	Kinetic
<ul style="list-style-type: none"> <li>• Time</li> <li>• Interval</li> <li>• Reads</li> </ul>	40:00 00:00:30 81
Absorbance Wavelength	340 nm
Plate Type	96 Well Standard clrbtm
Shaking before	5s Orbital, Medium
Shaking between	5s Orbital, Medium
Speed Read	On
Reading Order	Row
Designation of blank	First value automatically set to zero

Table 1. *Microplate reader parameters*

### 2.2.3 Conductivity measurement

To perform conductivity measurements on MTs solution we used a conductivity meter (Thermo Scientific™ Orion Star™ A212, Figure 3). Since BRB80 buffer has a high conductivity and would not be easy to identify great differences with MTs solution, we used BRB4 as well, diluting BRB80 and MTs solution obtained with BRB80, 20 times with Milli-Q water.

This measurement was performed reaching 4 ml of liquid inside a little beaker and by inserting the electrode in it. This device records accurate and reliable conductivity, total dissolved solids, salinity, resistivity and temperature measurements. First, we did the conductivity calibration using a conductivity standard with conductivity 1413 uS/cm. We prepared the conductivity cell according to the instructions in the conductivity cell use guide and rinsed it with distilled water, blot dry with a lint-free tissue and place into the standard, then we pressed start and waited for the conductivity value on the meter to stabilize and stop flashing.

Once the device was calibrated, we proceeded with the sample's measurement. We rinsed the conductivity cell electrode with distilled water again and blot dry with a lint-free tissue and place into the sample. Then we started the measurement and wait for it to stabilize. We collected all the data and then we removed the conductivity cell from the sample, rinse with distilled water, blot try and place into the next sample. We performed these measurements with buffers and MT solutions.



Figure 3. A212 Conductivity Benchtop Meter and the electrode

## 2.3 Results

### 2.3.1 Turbidity measurement

The biological activity of T240 is assessed by a tubulin polymerization assay. The ability of tubulin to polymerize into microtubules can be followed by observing an increase in optical density of a tubulin solution at OD340nm (see Figure 4).

Polymerizations were carried out as indicated in the Method. The three phases of polymerization are Phase I: nucleation (0-200 seconds), Phase II: growth (200- 1000 seconds) and Phase III: steady state (1000-3600 seconds). These phases can be seen only in the tubulin sample without the addition of Taxol. To examine the relationship between predictors and a response variable and to define the best model of the relationship, the curves were fitted with a sigmoidal model, through the Boltzmann equation. In vitro MT polymerization and dynamics are highly dependent upon reaction conditions such as temperature, glycerol concentration, and Mg<sup>2+</sup> concentration. For example, tubulin will polymerize at 37°C and depolymerize at 4°C. Paclitaxel binds to an internal region on MTs and stabilizes them against depolymerization both in vivo and in vitro.

As we can see in Figure 4, Taxol let the microtubules to form skipping the nucleation phase and stabilizing the microtubules after around 1000 seconds. The addition of this drug allows us to obtain a population of stable MTs at room temperature for 3 days and thanks to this we could work on these MTs and proceed with next measurements and characterization. These measurements have been repeated 3 times.

### 2.3.2 Conductivity measurement

The aim of the second measurement was to calculate the conductivity of the MTs

coated with gold nanoparticles and the background of this solution, in order to quantify the conductivity due to the MTs coated with Au NPs compared to the buffer. This was done thanks to the A212 Conductivity Benchtop Meter. We performed the measurements considering both BRB80 and BRB4, that is BRB80 diluted 20 times in DI-water. As we can see from Table 2, BRB80 has an order of magnitude higher in conductivity compared to BRB4. The MTs solution measured was diluted 20 times as well, to better identify the influence in conductivity of MTs and gold nanoparticles in the solution. The instrument gave the results very quickly and it gave the measurements also of the Resistivity, Salinity and Total Dissolved Solids. We measured the MTs coated with gold nanoparticles in the buffer with the presence of Taxol, diluted 20 times and the buffer by itself with the same dilution in DI-water. From the results obtained we can see that the presence of Taxol concurs to decrease the conductivity of the buffer by about 20  $\mu\text{S}/\text{cm}$ . While the MTs with gold nanoparticles cause an increase in conductivity of about 30  $\mu\text{S}/\text{cm}$ .

The results of these conductivity measurements confirm the influence of the buffer on the electrical properties of MTs. Indeed, as described in recent studies,<sup>15</sup> outside the microtubules there is the formation of a counterionic condensation which is strongly dependent on the buffer ionic concentration. In the case of BRB4, thanks to the dilution, the ionic concentration of the buffer is 8 mM, thus we are in a low concentration regime (10  $\mu\text{M}$  to 10 mM), and as also confirmed from Santelices et Al 2017<sup>16</sup>, in this case the microtubules increase the conductivity of their background. On the other hand, if we have BRB80 (ionic concentration 160 mM), it is representative of the physiological concentration regime (100-500 mM) and as confirmed from Kalra et Al. 2020b<sup>17</sup>, in these conditions, the microtubules decrease the conductivity of the background. In our case we didn't measure the conductivity of MTs in BRB80, but considering the high result founded for the buffer itself compared to the one diluted, we can assume our results as consistent.

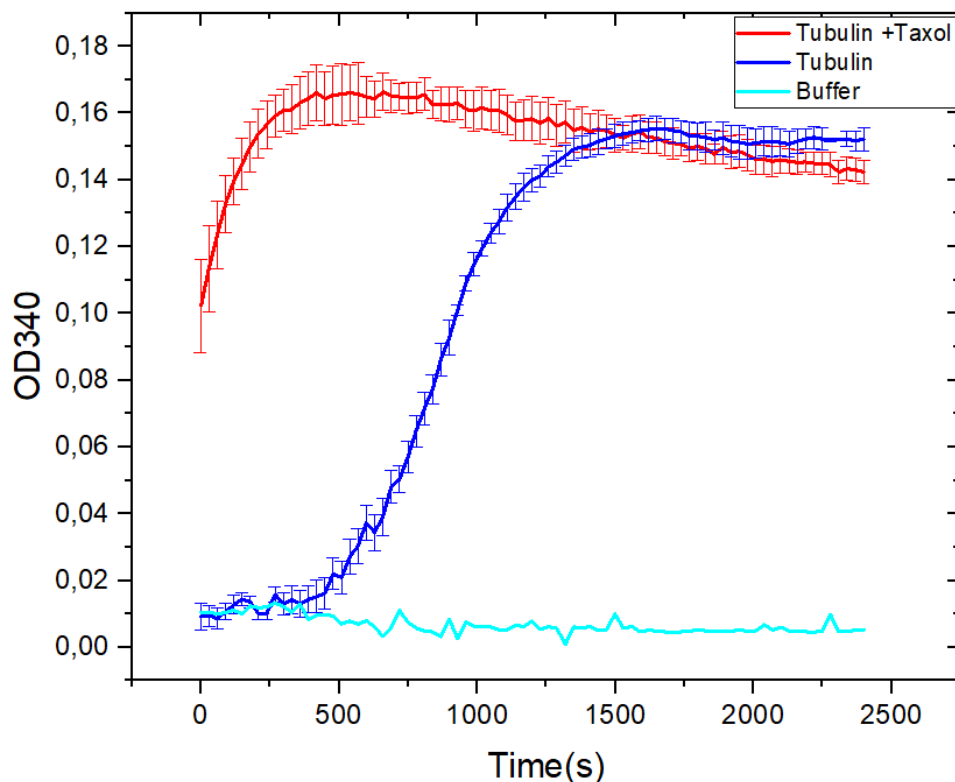


Figure 4. Standard polymerization reactions alone (Tubulin) and in the presence of 20  $\mu\text{M}$  paclitaxel (Tubulin + Taxol). A control with Buffer solution has been analyzed as well. Taxol causes rapid tubulin polymerization.

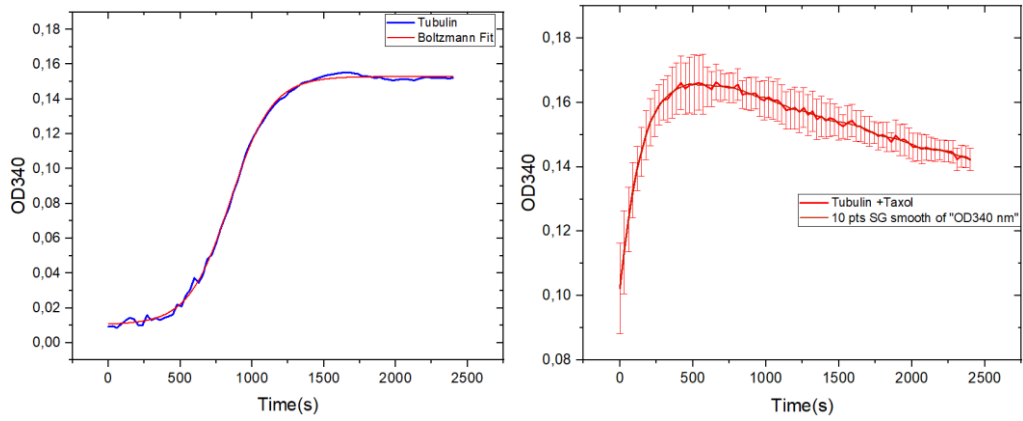


Figure 5. *a. relative Boltzmann fitted curve of tubulin solution turbidity measurement*  
*b. smoothed curve of turbidity measurement of tubulin solution + Taxol.*

	Conductivity	TDS	Salinity	Resistivity
<b>BRB80</b>	8.111 mS/cm	3.975 ppt	4.544 psu	123.3 ohm·cm
<b>BRB4</b>	510 $\mu$ S/cm	250.8 ppm	0.297 psu	1.958 Kohm·cm
<b>MTs Solution + Taxol</b>	520.5 $\mu$ S/cm	255.5 ppm	0.302 psu	1.921 Kohm·cm
<b>Buffer + Taxol</b>	489.3 $\mu$ S/cm	240.3 ppm	0.286 psu	2.044 Kohm·cm

Table 2. *Conductivity results on A212 Conductivity Benchtop Meter for MTs solutions and relative buffers.*

# Chapter 3

## 3 Gold nanoparticles coated microtubules

### 3.1 Gold nanoparticles coating goals

Tubulin molecules have specific patterns of amino acid side chains on chemically reactive surfaces that offer a range of active sites for the nucleation, organization, and binding of metal particles.

The synthesis of nanoscale systems via alternative methodologies is primarily motivated by commercial needs to generate progressively tiny structures, such as components for microelectronic devices. The typical size dimensions of biomolecular structures vary from the lower nanometer size range to several micrometers, together with clearly defined surface capabilities. Because of their molecular recognition capabilities, many among them have interesting characteristics, for instance, they can be able to self-assemble into complex, well-defined, and extended superstructures.<sup>18</sup> However, it's not easy to work with biological systems, because, despite the excellent capabilities already cited, they don't display the appropriate physical characteristics when it comes to intrinsic electric conductivity. Thus, one of the aims in our work, was to use microtubules as a template where to photodeposit spherical gold nanoparticles, in order to give them further interesting and useful features for example for future integrated circuits.

Photochemical reduction methods were employed to form Au nanoparticles which bind and uniformly cover the MT filaments.<sup>19</sup> UV/vis and Raman spectroscopy were used to characterize the MT-templated Au nanowires' synthetic process. Raman discovered numerous functional groups that could communicate with the Au. The findings from this research help us understand how gold binds to the biotemplate and shed light on how to increase gold coverage for MT-templated gold nanowires.

### 3.2 Materials and methods

#### 3.2.1 Photodeposition

Photodeposition technique was used to deposit gold nanoparticles (AuNPs) on the surface of the synthesized MT samples. The gold precursor consisted of HAuCl<sub>4</sub> dissolved in methanol. 20  $\mu$ L of 25 mM HAuCl<sub>4</sub> was dropped and mixed properly using magnetic stirrer and exposed under UV curing lamp of 365 nm wavelength for 30 minutes. The MTs changed in color from transparent to bluish purple, indicating the successful deposition of AuNPs.

#### 3.2.2 Uv-vis

The sample obtained after UV exposure is shown in Figure 6. The mixture was transferred to UV cuvettes and characterized with the spectrophotometer UV vis (Hitachi U-3900H). UV-vis spectroscopy performed in the range of 200 - 800 nm under transmission mode.

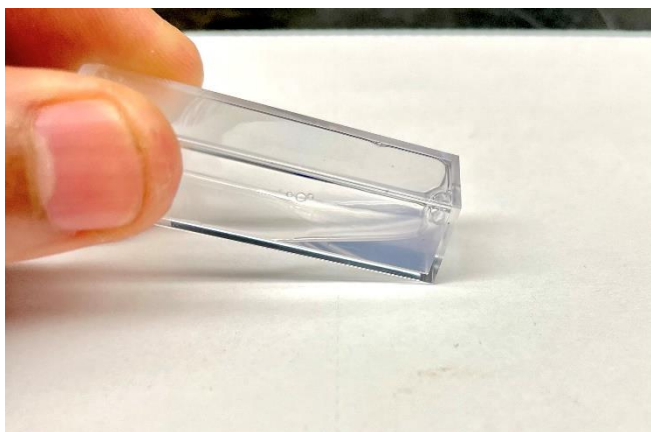


Figure 6. *Sample for UV vis, obtained from photodepositon, through UV curing lamp at 365 nm of H<sub>AuCl</sub>4 on microtubules.*

### 3.2.3 RAMAN Spectroscopy

The sample has been rinsed and used for Raman spectroscopy (Figure 7). Raman spectra were obtained using a Renishaw inVia Raman microscope (Figure 8). This type of technique is one of the most powerful for characterizing the interaction between metal and protein functional groups. Surface plasmon excitation on roughened metal surfaces such as Ag, Au, and Cu selectively increases (up to 109 times) the vibrational modes of only those molecules that are close to the roughened metal surface and for this reason it offers a very sensitive detection of the absorption of functional groups by these metals.<sup>20</sup> These interactions have been studied for a long time, however, in most of these investigations, they focus only on the absorption only in short peptides that with only a few potential binding sites.<sup>19</sup> In our experiments we used 532 nm laser, 1200 lines per mm grating, 100% power, exposition time 1s, with X50 objective lens.

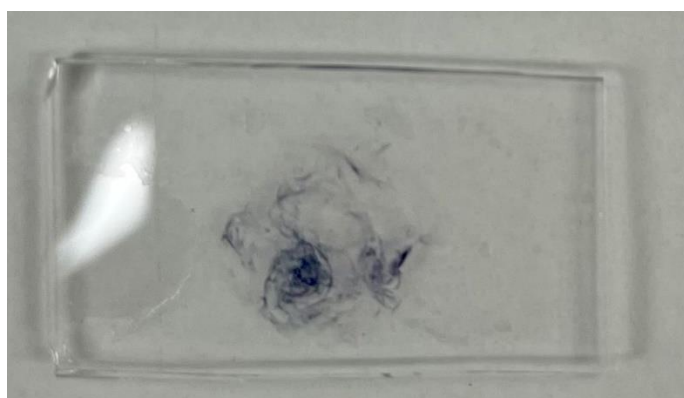


Figure 7. *Sample for Raman Spectroscopy*



Figure 8. *Renishaw inVia Raman microscope*

### 3.2.4 KEITHLEY Measurement

The instrument that was used to measure the impedance of our samples was provided by an ex-researcher student from the University of Alberta. This section reports on the building procedure. Glass slides coated with FTO (Fluorine-doped Tin Oxide) used for each "plate" in the parallel-plate contact device (Sigma Aldrich, 735140). The slides were cut to have top contact dimensions of 1.5 mm x 10 mm x 50 mm and bottom contact dimensions of 1.5 mm 27 mm x 50 mm. To eliminate surface particulate matter, the slides were ultrasonically cleaned and then treated to Reactive Ion Etching (RIE) utilizing a 5-minute exposure to oxygen plasma (Oxford Instruments, NGP80). He used a double-sided tape that is 70 mm thick to create a chamber that is 3 mm by 1.25 cm by 70 mm in size and a different 3D-printed holder device was used to position the upper electrode, (Figure 9) <sup>4</sup>.

Having the device constructed with the above protocol, experiments were conducted using Impedance Spectroscopy on Keithley 4200-Semiconductor Characterization System (SCS Analyzer) (Figure 10).

We set CVU options, connecting the CV high potential cable to the collector number 4 (the one on the right in Figure 10) and the CV low potential to the collector 1 (on the left). We used a copper alligator clips to bind the collector 1 and the upper glass of the parallel-plate device, whereas the common electrode was attached at the lower glass. We set the frequency sweep option and 0 bias was introduced. Solutions were perfused into the experimental chamber using a micropipette tip at one opening, and a filter paper at the other opening for suction the excess. The frequency range of the measurement was set from 1 kHz to 10 MHz and data were subsequently collected.

After each data collection and before the next one we washed the chamber with buffer, BRB4, or BRB80. We also paid attention to any bubbles that could form in the chamber during the measurements, eliminating them and repeating the measurement, if necessary, in order to avoid any alterations in the results.

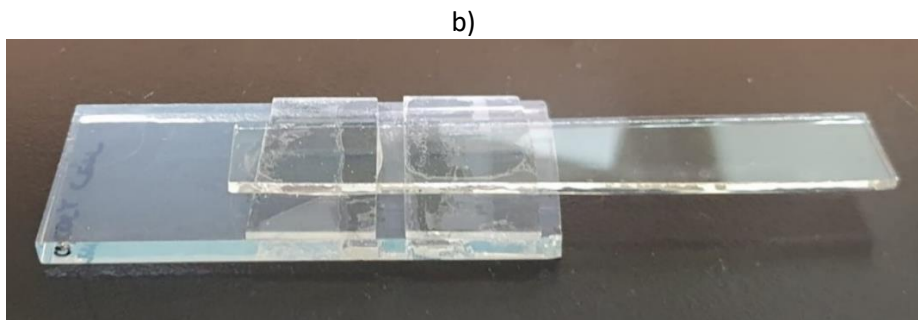
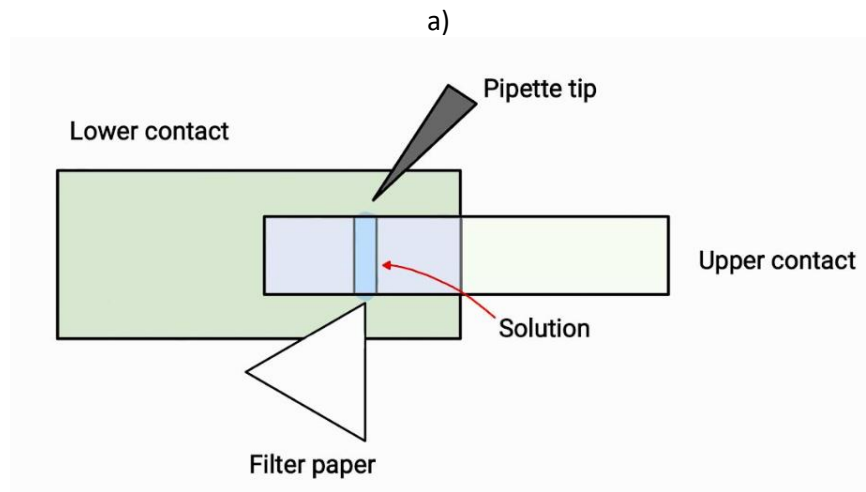


Figure 9. A parallel-plate contact device to measure the impedance properties of MTs coated with Au nanoparticles compared to background. a) schematic figure; b) the device.

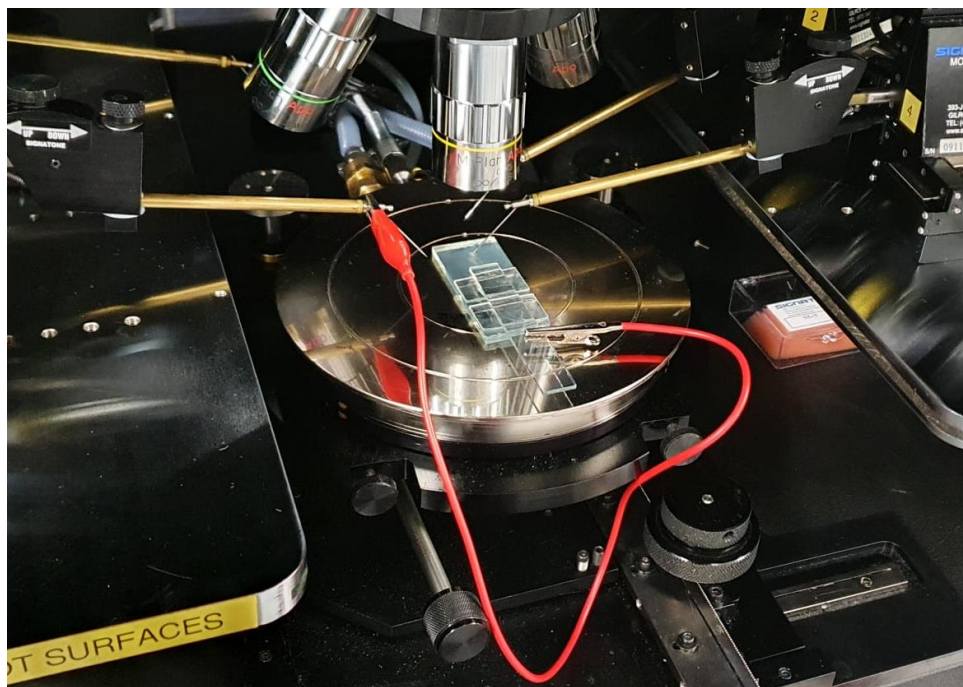


Figure 10. Keithley 4200-Semiconductor Characterization System set-up

## 3.3 Results

### 3.3.1 UV-vis

In this study we used UV-vis spectroscopy to characterize the Au nanoparticles formed on the microtubules and in Figure 11 is reported the UV/vis spectrum of the solution containing MT, HAuCl<sub>4</sub> after 5 min exposure. Different studies showed that UV-vis spectra of solution containing HAuCl<sub>4</sub> UV-vis absorption measurements present a peak at 520 nm indicating the formation of Au nanoparticles on the filaments<sup>21,22</sup>. In this work we measured the absorption of MTs solution with HAuCl<sub>4</sub> coated on them and in Figure 11 we reported results. We can see the presence of a broad peak at 520 nm, and it suggests us that the formation of Au nanoparticles on the filaments worked, but in a fewer concentration and less monodisperse. We expect that some of the UV irradiation is absorbed by the MT proteins.

Since we observed this peak, we can confirm that the results are consistent with previous analysis, and we could go on using these samples for Raman measurement because we expected that the aggregation of colloids could give us a better Raman signal.

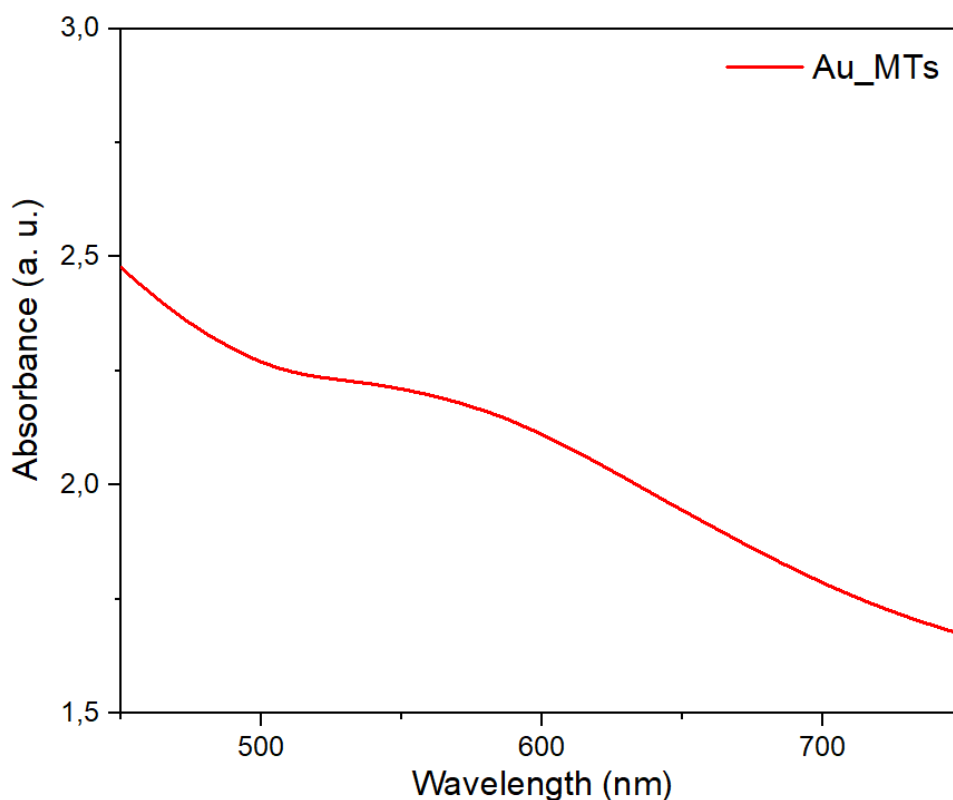


Figure 11. Broad peak at 550 nm obtained from UV-vis analysis

### 3.3.2 RAMAN

The Raman spectrum of the Au decorated MT sample showed multiple peaks, which were all caused by interactions between the functional groups on the MT and the Au surface. In order to clearly demonstrate that the vibrational modes are indeed amplified in the Au adorned MTs as compared to the two control samples that have been studied and published in other studies, we focused on the region between 1450

$\text{cm}^{-1}$  and  $1630 \text{ cm}^{-1}$  shown in Figure 12.<sup>19</sup>

The imidazole group-containing histidine residues are presumably the main factor in the Au binding. In fact, four histidines that are conveniently accessible from the solution are centrally placed on the tubulin surface of  $\alpha\beta$ -tubulin dimers in the crystal structure. Hence, the imidazole ring is predicted to be the main mechanism by which gold will attach to histidine residues as it is generally known that imidazole groups can coordinate to several different metal ions in biological reactions, and it has been demonstrated that histidine-rich peptides can bind to gold nanoparticles and diminish  $\text{Au}^{3+}$ . The imidazole ring's imine is normally protonated but is deprotonated at physiological pH. It is widely acknowledged that histidine coordinates through the basic imine and, on occasion, the nitrogen center of the basic imine of the imidazole ring.<sup>19</sup>

Spectra in the region from  $1450 \text{ cm}^{-1}$  and  $1630 \text{ cm}^{-1}$  shows enhanced vibrational modes and we assumed that the peak at  $1505 \text{ cm}^{-1}$  and  $1520 \text{ cm}^{-1}$  are assigned to  $\text{NH}_3^+$  symmetric deformation mode, and the peak at  $1570 \text{ cm}^{-1}$  is the C=C stretch of the imidazolium ring.

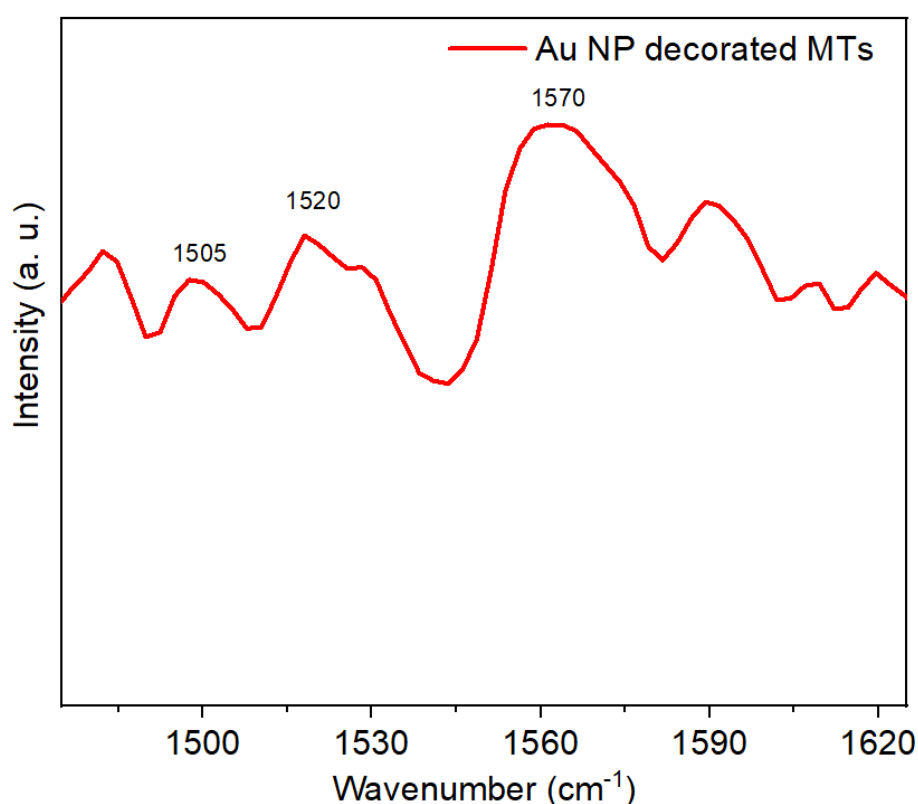


Figure 12. Raman spectra for the gold–MT system

### 3.3.3 KEITHLEY

Once demonstrated, through the characterizations described above, that the gold nanoparticles have successfully formed on the microtubules, we proceeded to our main experiment.

Our sample solutions were perfused into the experimental chamber using a micropipette tip at one opening and the data were collected in a range of frequency from 1 kHz to 10 MHz.

From Figure 13 we can observe the differences in impedance and in phase for the MT

coated with gold nanoparticles and the respective buffers. Successively we have subtracted the impedance values of the media from the ones of the solutions, to evaluate better the differences. The impedance in the case of BRB80 is very low, ( $\sim 10^2$ ) and it does deeply influence the MT with gold nanoparticles in it. In Figure 15. is also shown the module of the admittance, in Siemens. As we can better see from these curves, BRB80 is more conductive than BRB4, as the conductance is the real part of the admittance. This is explained by the fact that ionic conductivity is proportional to the number of charge carriers, so the local conductivity can be equated with the local ionic concentration. Indeed, the BRB80 has an ionic concentration of 160 mM, while BRB4, 8 mM, as it is 20 times diluted BRB80.<sup>15</sup> Moreover, the fact that microtubules with gold nanoparticles, in BRB80 buffer increases the impedance of the solution, and so decrease the conductance, is linear with the results of Kalra et al 2020b<sup>17</sup>. On the other hand, in previous experiments, when the buffer ionic concentration was in a low concentration regime (10  $\mu$ M to 10 mM), so for example, in the case of BRB4, the microtubules-ion complex could be clearly distinguished as a highly conductive wire in a non-conductive medium. In our case, instead, despite expectations, we found that microtubules with gold nanoparticles decrease increase the impedance of the media. In particular, we can notice that the BRB4 has impedance of order  $\sim 10^3$ , while the microtubules in this buffer increase the impedance of  $\sim 90$ %. In both cases seems that the medium deeply influences the total conductivity, but considering previous works, where was demonstrate that microtubules in low conductive medium could be considered as conductive wires, we found that the gold nanoparticles in our biotemplates, nullify this behavior contributing instead to resistance features. In addition, we subtracted the data of the medium from the total solution, considering the microtubules in parallel with the media, and we calculated the real and imaginary part of the impedance, obtaining the graphs in Figure 14 and 16, respectively.

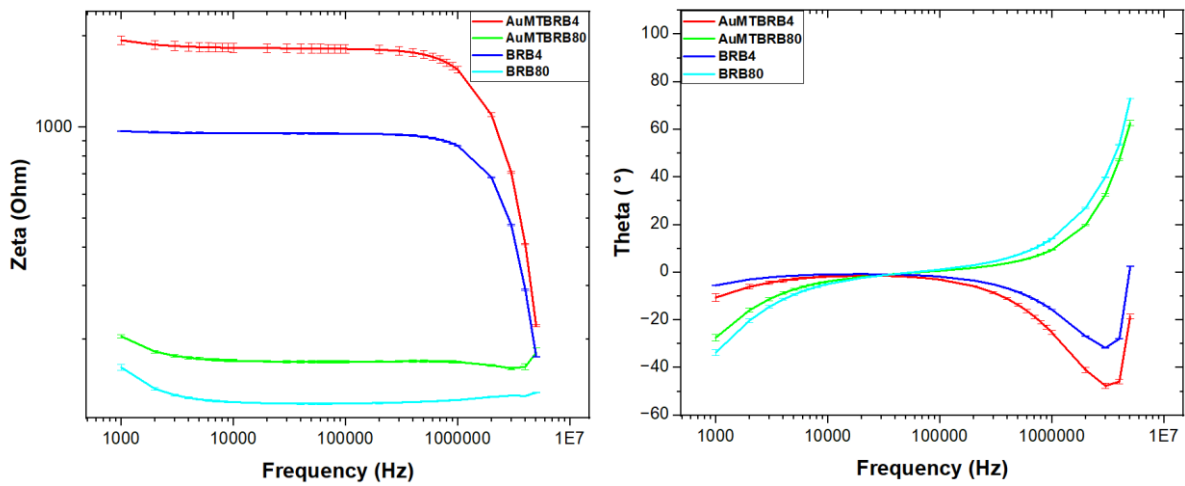


Figure 13. Impedance and Phase of the sample solutions.

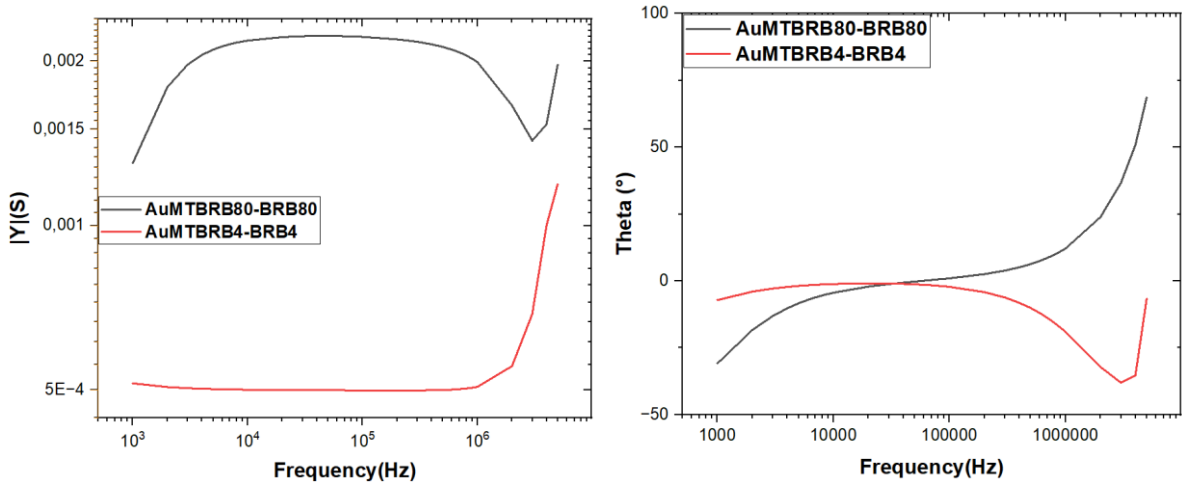


Figure 14. Impedance and Phase of the sample solutions subtracting the medium data from the total solution.

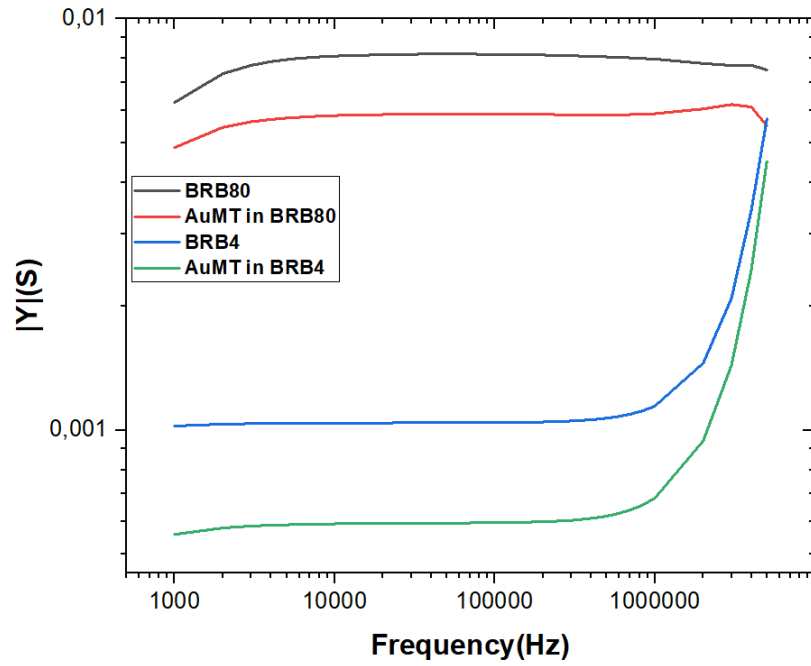


Figure 15. Module of the admittance of our samples.

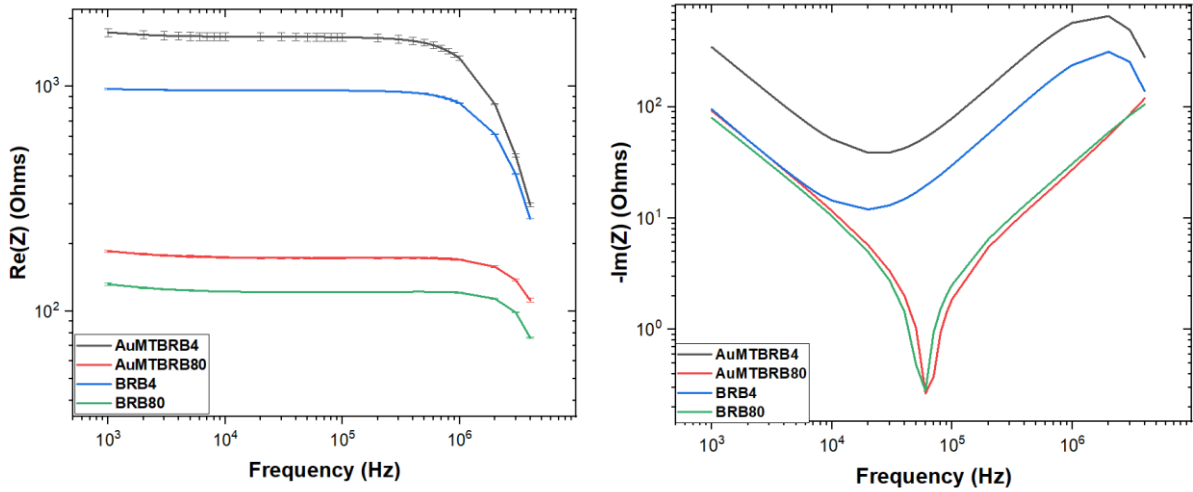


Figure 16. Real and imaginary part of the magnitude of the impedance.

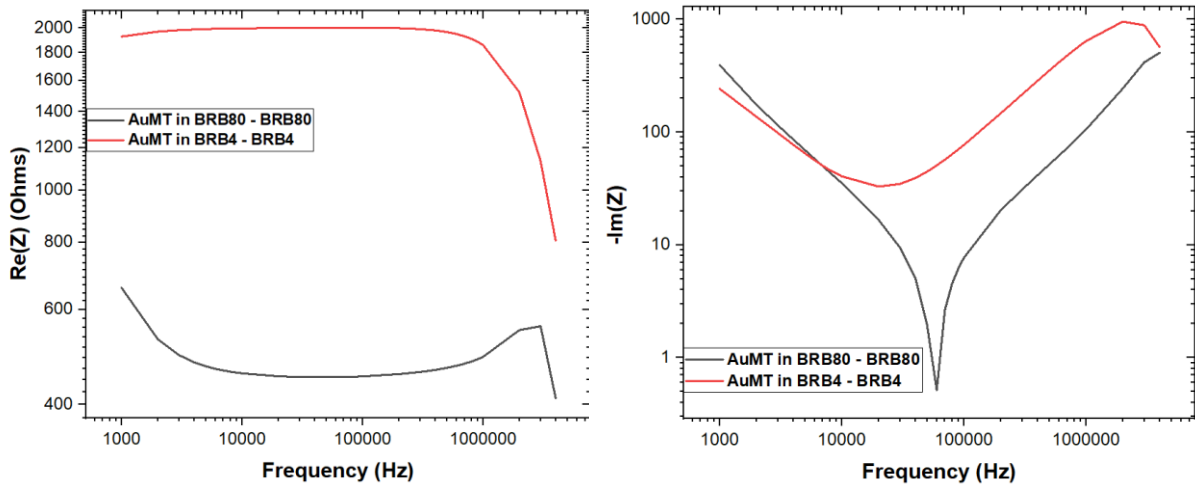


Figure 17. Real and imaginary part of subtracting the media.

### 3.3.4 Data Analysis

In this section we will model our solutions as a circuit formed by resistance and capacitive components, considering the value of capacitance and resistance calculated from the real and imaginary part of the impedance's curves previously obtained through our measurements.

We considered the microtubules as filament of  $\sim 10 \mu\text{m}$  in length, as suggested by the protocol we followed, and considering the 13 protofilaments formed by tubulin dimers long 8 nm each, we could calculate the number of tubulin dimers in 1 protofilament ( $N_d = 1250$ ) and the number of tubulin dimers in 1 MT ( $N_m = 16250$ ).

$$N_d = \frac{10 \mu\text{m}}{8 \text{ nm}} = 1250;$$

$$N_m = 13 * 1250 = 16250$$

The concentration of the tubulin in the microtubule's solution in BRB80 was 22,7  $\mu\text{M}$ , which corresponds to 1,8 nM microtubules, while the one in BRB4 was 1,135  $\mu\text{M}$ . The volume of the chamber where the conductance measurements were performed was 2,625  $\mu\text{l}$ , and so the total number of tubulin dimers is considered around  $\sim 35,7 \times 10^{12}$  and around  $\sim 1,5 \times 10^{12}$  in BRB80 and BRB4 respectively.

In conclusion the number of MTs in the chamber of the conductance measurements was  $\sim 2,197 \times 10^9$  and  $9,477 \times 10^7$ .

$$N_{MTBRB80} = \frac{35,7 * 10^{12}}{16250} = 2,197 * 10^9;$$

$$N_{MTBRB4} = \frac{1,5 * 10^{12}}{16250} = 9,477 * 10^8;$$

The model we propose to characterize the MT coated with gold nanoparticles is a complex RC circuit characterized by percolated resistances or capacitances, depending on the frequency.

Our next goal was to calculate a single MT's electrical characteristics using the results of our studies. Impedance difference curves had a slope of around negative unity on log-log plots and were linear (Figure 16), indicating that the MTs meshwork added a capacitive component to the solution, and it was linear with other researches <sup>4</sup>. Different combinations of RC circuit were examined to better fit our results and ideas, and a model of it is reported in Figure 18.

The net impedance of the background (BRB80 or BRB4) was given by:

$$Z_{buffer} = Z_o + Z_s$$

Where  $Z_o$  is the impedance due to external circuit element and  $Z_s$  the impedance of the solution (BRB80 or BRB4). Denoting the impedance, resistance, and capacitance of the entire MT meshwork by  $Z_{MT}$ ,  $R_{MT}$  and  $C_{MT}$  respectively, and considering two additive resistances for the tubulin monomers not polymerized and for the gold nanoparticles not attached,  $R_H$  and  $R_G$  respectively, the impedance for the circuit with MTs is given by:

$$Z_{MT+buffer} = Z_o + Z_s + R_H + R_G + \tilde{Z}_{MT}$$

In this case we are assuming that the impedance  $Z_{MT}$  include both the total impedance given by the microtubules and the gold nanoparticles attached to them. To determine the capacitance and resistance of a single MT coated with the gold nanoparticles from corresponding meshwork mean values, we made 2 further assumptions. (1) The average length of an MT was taken as 10  $\mu\text{m}$  and (2), MTs were oriented in parallel to one another at our concentration. In Table 3 are reported the values of capacitance, resistance of the entire MT meshwork and of the respective buffers, calculating with the following formulas, in which we used the values of the real and imaginary part of the impedance from the curves in Figure 16. We considered  $w_i$  the lower value of frequency available in our measurements.

$$Z = \sqrt{Re^2 + Im^2}$$

$$\tilde{R}_{MT} = Re(Z)$$

$$\tilde{C}_{MT} = \frac{1}{Im(Z) * w_i}$$

	$\tilde{C}_{MT}$ (F)	$\tilde{R}_{MT}$ ( $\Omega$ )	$\tilde{C}_{buffer}$ (F)	$\tilde{R}_{buffer}$ ( $\Omega$ )
<b>AuNP-MT in BRB80</b>	10,9 x 10 <sup>-6</sup>	184,97	12,6 x 10 <sup>-6</sup>	131,7
<b>AuNP-MT in BRB4</b>	2,546 10 <sup>-6</sup>	1744,45	10,568 10 <sup>-6</sup>	976,08

Table 3. Resistance and capacitance of the entire MT meshwork and of the respective buffer.

Considering the MTs in parallel to each other and with the media, we obtained the curves of Figure 17, and we used that data to find the resistive and capacitive contribute of all the MTs without the buffers. The values are reported in Table 4.

	$\tilde{C}_{MT}$ (F)	$\tilde{R}_{MT}$ ( $\Omega$ )
<b>AuNP-MT in BRB80 – BRB80</b>	2,54 x 10 <sup>-6</sup>	393,76
<b>AuNP-MT in BRB4 – BRB4</b>	4,13 10 <sup>-6</sup>	242,18

Table 4. Resistance and capacitance of the MT meshwork subtracting the buffer.

Given the presence of  $N_{MTBRB80} = 2,197 \times 10^9$  MTs and  $N_{MTBRB4} = 9,477 \times 10^8$  MTs in our solution at respectively 22,7  $\mu$ M and 1,135  $\mu$ M concentration, the capacitance for a single 10  $\mu$ m long MT with gold nanoparticles, in BRB80 was calculated to be  $C_{BRB80} = C_{MT}/N = 1,156 \times 10^{-15}$  F.

While for the MT in BRB4  $C_{BRB4} = C_{MT}/N = 4,358 \times 10^{-15}$  F.

We extended our set of assumptions to calculate the resistance of a single 10  $\mu$ m long MT at different concentration. Here, the total resistance of the MT meshwork would be given by  $R_{MT}$ , while each MT has resistance  $R_{MTBRB80} = R_{MT}/N = 1,792 \times 10^{-7}$   $\Omega$  and  $R_{MTBRB4} = R_{MT}/N = 2,555 \times 10^{-7}$   $\Omega$ .

The results of the resistance's contribute are really close in both cases, but the microtubules in BRB80 are more conductive than in the one of diluted buffer, so even if we subtracted the media contribute, the buffer seems to have some effect. Probably this is due to the fact that we considered all the microtubules in parallel with each other, thus a more accurate model is needed.

To determine if these values were consistent with theoretical predictions, the total capacitance of the MT cylinder has been calculated by previous models to be given by<sup>23</sup>:

$$C_{MT,teor} = \frac{2\pi\epsilon_0\epsilon_l l}{\ln(1 + \frac{\lambda_D}{r})}$$

Where  $l$  is the length of the microtubule,  $\epsilon_r$  is the relative permittivity.  $\lambda_D$ , defined as Debye length, which is given by

$$\lambda_D = \sqrt{(\varepsilon_0 \varepsilon_r k_B T) / (2 N_A c_s e^2)}$$

is a measure of how far into the plasma the potential of an electrode or probe is observed, and it depends on the concentration.  $\varepsilon_0$  is the permittivity of free space,  $k$  is Boltzmann's constant, and  $q$  is the charge of the electron. Normally, if we have a negative charged microtubule, positive ions tend to congregate around it, and the Debye length is the distance of how far its electrostatic effect persists.

While the relative permittivity in the NLPB and LPB equations is often assumed to have a constant value, usually  $\varepsilon=80$  which the value for water, this assumption is not entirely accurate. For our calculation we will consider then a variable relative permittivity using the work of Lamm and Pack (1997).<sup>24</sup> According to these studies, for cylinders, the effect of surface geometry on the local relative permittivity was negligible compared to the Booth and concentration effects.<sup>15</sup> Considering that the relative permittivity from the surface of the protein varies from 3 to 80, considering the closest neighborhood to the protein it should be in a range between 3 to 10. In our experiments we will assume  $\varepsilon_r=5$ .

The capacitance is an electric component that depends on the inverse Debye length through the electric potential and considering that this distance depends on the ionic concentration, we will use 2 different values for  $\lambda_D$  for characterize our solutions.

The Debye length under physiological conditions, so for ionic concentration buffers from 100 to 500 mM, is  $\approx 0.8$  nm. While at low ionic concentration  $\lambda_D$  can be very long<sup>15</sup>. Considering our microtubules long 10  $\mu\text{m}$  and with ratio  $r=12,5$  nm, substituting the values in the previous formula, we find that the theoretical capacitance of 1 MT coated with gold nanoparticles in BRB80 is  $C_{MTBRB80, \text{teor}} = 4,48 \times 10^{-15} \text{F}$ . If we suppose the Debye length for low ionic concentration is 5 times greater, we obtain  $C_{MTBRB4, \text{teor}} = 8,3 \times 10^{-15} \text{F}$ . In Table 5 is reported the comparison between the experimental and the theoretical values.

Thus, in conclusion we can say that the final results are almost linear with the predictions, and in particular, the ionic concentration of the buffer influences the capacitive contribute of a single MT with gold nanoparticles. Moreover, we can suppose that the gold nanoparticles on the microtubules have an effect on it as well, such as the capacitive contribute in presence of BRB80 is lower than the theoretical value, while in a diluted buffer, it is 4 times higher.

Nevertheless, more experiments are required to better clarify their role.

	$\tilde{C}_{MT, \text{exp}} \text{ (F)}$	$\tilde{C}_{MT, \text{teor}} \text{ (F)}$
<b>1 AuNP-MT in BRB80 – BRB80</b>	$1,156 \times 10^{-15}$	$4,48 \times 10^{-15}$
<b>1 AuNP-MT in BRB4 – BRB4</b>	$4,358 \times 10^{-15}$	$0,83 \times 10^{-15}$

Table 5. Comparison between the experimental and the theoretical value for the capacitive contribute of a single MT.

#### Creation of a model

As mentioned before, to subtract the data of the media from the MT solutions, we have considered microtubules in parallel with each other, and with the media as well. A possible scheme of the circuit is represented in Figure 18, where  $Z_0$  is the impedance of the external elements,  $Z_s$  the one of the solutions,  $R_h$  is the small constant

resistance that represent the small fraction of unpolymerized tubulin and  $R_g$  the possible presence of gold nanoparticles, that didn't attach to the MTs, in the solution. This is a RC circuit, and we tried to give a further explanation to what were the meaning of our curves, comparing them to previous works on conduction flow-paths through random composite media.<sup>25</sup>

We observed our data and we noticed that in the case of BRB4 and microtubules in BRB4, our curves presented similar trends compared to the response of percolated resistors networks, described in the work just cited. On the other hand, the solutions with BRB80 had different behavior. The graphs of the phase could be considered similar to the system characterized by percolated resistance at low frequencies and percolated capacitors at high frequencies. The reason of this difference may be due to the great conductivity role, since BRB80 has a high ionic conductivity.

Nevertheless, more studies are needed, to better clarify these features and find the perfect model to this system.

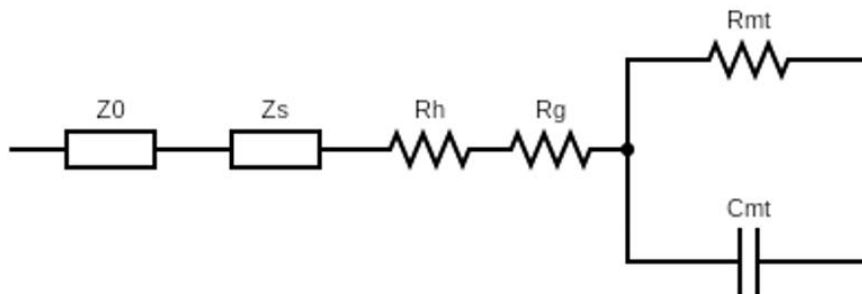


Figure 18. *The equivalent electrical circuit model representing the microtubule meshwork as a parallel RC circuit, with meshwork resistance  $R_{MT}$  and capacitance  $C_{MT}$ . The external element has impedance  $Z_0$ , while solution has impedance  $Z_s$ .  $R_h$  is the small constant resistance that is ascribed to small fraction of unpolymerized tubulin that is present in MT containing solutions.*

# Chapter 4

## 4 Actin

### 4.1 Exploit Actin features

Since Straub's discovery of actin in muscle tissue in 1942<sup>26</sup>, actin has been proven to be the most prevalent cytoskeleton protein in many eukaryotic cells. Actin also performs a wide range of crucial cellular tasks, including cell motility and the finding and transport of protein complexes. Actin performs these functions through a process known as actin dynamics, which involves the dynamic building and disassembly of structures including lamellipodia and filopodia. Between polymerized F-actin and monomeric G-actin, actin is in a dynamic equilibrium. One adenosine nucleotide is tightly bound by actin, and the polymerization brought on by the change from G to F-actin activates the ATPase.<sup>27</sup>

Actin in its monomeric form is a globular protein of 42 kDa, roughly 5.5 nm in diameter.<sup>28</sup> It is slightly acidic and is made up of a single polypeptide chain with 375 amino acids. Actin has two domains divided by a cleft that binds two cofactors: an ATP or ADP-compatible nucleotide and a calcium- or magnesium-compatible cation. Subdomains I, II, III, and IV are each one of the two domains' two additional subdomains. The accessible side of subdomains I and III is referred to as the monomer's barbed end or (+) end, and the accessible side of subdomains II and IV is referred to as its pointed end or (-) end. When put in the presence of a nucleotide and a divalent cation at physiological salt concentrations, monomers can spontaneously join to form filaments. New molecules often join at the (+) end of an existing F-actin strand as the threads get longer. On the other hand, threads often contract by losing actin monomers from the (-) end of the strand.

The nucleotide state and the type of metal ion have a significant impact on the dynamics of filament creation and stability. These filaments of actin, denoted as F-actin are 37 nm-thick linear chains of actin monomers organized in two actin helical strands that are twisted around one another to form a 7 to 9 nanometer diameter helix that repeats every 72 nanometers (or every 14 G-actin subunits). G-actin molecules are all pointed in the same direction in F-actin threads. The F-actin thread has two unique ends that are separate from one another.<sup>29</sup>

Actin monomers assemble in a polar manner with barbed faces pointing in the same direction. As a result, the filament's two ends reveal two different faces of the final actin monomer, giving it polarity and exposing a barbed and a pointed monomer face at each end.<sup>30</sup>

G-actin molecules can polymerize into longer filaments under a variety of circumstances and these filaments that are formed, are both strong and dynamic.

In opposition to other polymers, as DNA, that are constitute by covalent bonds, the monomers of actin filaments are assembled together by weaker bonds, that can be easily broken by thermal agitation. Nevertheless, the filament ends have the advantage of being able to release or incorporate monomers readily because of the lateral connections with nearby monomers. This indicates that in response to an external stimulation, the filaments can quickly remodel and alter cellular structure. This behavior is also known as the "assembly dynamic".<sup>31</sup>

Under physiological conditions, actin filaments can be considered as polymers that behave as highly charged polyelectrolytes<sup>32</sup>. The linear charge density of F-actin is estimated theoretically to be  $4 \times 10^3$  e/ $\mu\text{m}$  in vacuum, and it may support ionic condensation-based waves in buffer solutions as originally predicted by Manning's

condensation theory<sup>33</sup>. In this, he stated that polyelectrolytes may have condensed ions in their surroundings. These ions are called counterions, and condense along the length of the polymer, if a sufficiently high linear charge density is present along the surface of the polymer. As we know actin filaments are highly negative charged, so according to this theory, there is the formation of this layer of ions that comes from the saline solution, and co-ions of this solution are repelled.

The sum of surface charges and related counterions is reduced to values determined by a formula based on counterion valence and Bjerrum length. This parameter, in turn, depends on the solvent and solution temperature and is a phenomenological property of the ion's capacity to balance the surface charges<sup>9</sup>. The Bjerrum length is the distance at which the Coulomb energy of the screened charges equals  $kBT$ , the thermal energy, creating an equilibrium from which the charges would not move.

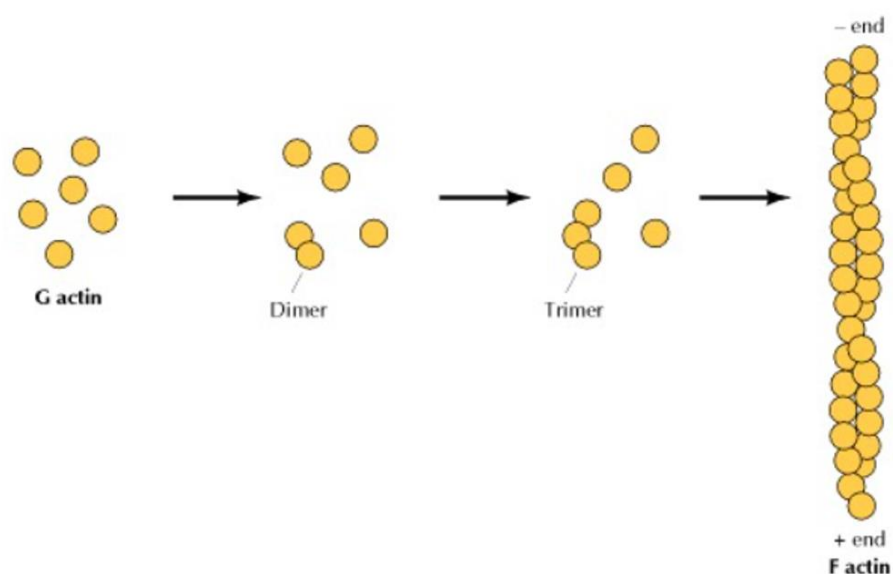


Figure 19. *The Cell: A Molecular Approach. 2nd edition.*

## 4.2 Materials and methods

### 4.2.1 Actin reconstitution

We reconstituted 1 mg and, subsequently, 0.25 mg of unlabeled lyophilized actin powder (Cytoskeleton, Actin Protein (>99% Pure): Rabbit Skeletal Muscle Cat. # AKL99) in 0.333 mL of DI-H<sub>2</sub>O, to obtain at the end different concentration of actin in solution. We then diluted it by adding 2.1645 mL of General Actin Buffer (Cytoskeleton, General Actin Buffer Cat. # BSA01) to reach 0.4 mg/mL in actin concentration and adding 5  $\mu$ l of ATP (Cytoskeleton, Adenosine 5'-triphosphate disodium salt (ATP) Cat. # BSA04, 100 mM stock) to yield a final ATP concentration of 0.2 mM. We then added 12.5  $\mu$ l of DTT 100mM to yield a final concentration of 0.5 mM of DTT to the actin solution and we incubate it on ice for 1 hour.

We centrifugated at 1400 RPM for 15 minutes at 4°C. We then divided our actin solution in aliquots of 100  $\mu$ l in volume and we assembled the polymerization reaction by adding 1/10th the volume Actin Polymerization Buffer (Cytoskeleton, APB at 10X Cat. # BSA02), so adding 10  $\mu$ l of APB to each aliquot. Finally, we added 1.1  $\mu$ l of ATP to each aliquot. The aliquot not needed for our analysis where snap frozen and stored at -80°C.

Following these steps from 2 vials of unlabeled lyophilized actin powder of 1 mg and 0.25 mg, we managed to obtain samples of actin solution at different concentrations, 0.35 mg/mL and 0.1 mg/mL respectively.<sup>34</sup>

#### 4.2.2 Actin polymerization

Once added ATP to each aliquot, we incubated the polymerization reaction at room temperature for 1 hour.

Actin polymerization is the mechanism by which force is generated in many cellular processes. While spontaneous actin polymerization is possible, cells maintain control over this crucial process by limiting actin filament nucleation and then permitting promoted polymerization and elongation by a number of controlled factors. In vitro reconstructions of actin polymerization, regulated nucleation, and controlled elongation activities can be utilized to investigate the signaling cascades that cells use to govern the timing and location of actin polymerization.<sup>35</sup>

Actin will form filaments whenever its concentration is higher than its critical concentration, which can be influenced by the type of actin, bound nucleotides, and a variety of solution circumstances. Thus, by eliminating practically all of the salts present, keeping it mildly alkaline, and adding calcium ions rather than magnesium ions, pure actin can be kept as monomers. Then, thanks to the addition of a concentrated buffer solution that changes the pH, flips the divalent cations, and raises salt concentrations into the physiological range, the solution can be induced to form filaments. In bulk solutions, the polymerization of actin can be monitored by observing a number of observables, such as the rise in light scatter or the viscosity of the solution as the polymers multiply.<sup>36</sup>

Actin filaments rapidly assembled and disassembled, and assembly classically occurs in three steps: nucleation phase, elongation phase and steady-state phase. First, two to three G-actin molecules slowly join to form a small oligomer that will nucleate further growth. Second, by adding several actin molecules to both ends, the actin filament quickly expands. Actin molecules are added to the plus end of the filament approximately 10 times quicker than to the minus end as the filament grows, which is why filaments often grow at the plus end. Third, actin molecules join and leave the filament at the same pace, achieving equilibrium and sustaining the filament's length. While the length of the filament remains constant in the steady-state phase, new molecules are continually being added to the (+) end and falling off the (-) end, a phenomenon known as "treadmilling" as a particular actin molecule appears to move along the strand. The amount of G-actin surrounding an individual filament determines whether it will grow or shrink and how quickly; nevertheless, in cells, different actin-binding proteins have a significant impact on actin filament dynamics<sup>6</sup>.

#### 4.2.3 Turbidity Measurement

Purified actin has been used to replicate actin polymerization in vitro so that the kinetics of the process can be studied apart from other proteins. Turbidity measurement can be used in to prove the polymerization of actin filaments.

We used the spectrophotometer previously cited (SpectraMax<sup>®</sup> iD5 microplate reader (Figure 3), and an optically clear vessel (multiwell plate). We quickly pipetted 100  $\mu$ l of the actin samples previously obtained into a 96 well plate and we performed turbidity measurement in 310 nm absorbance kinetic mode for 60 minutes at 25°C<sup>37</sup>. 81 points have been obtained, one every 30 seconds and before each reading the plate was shaken. All parameters are reported in Table 6.

Actin assembly is characterized by a short lag time, a period of net increase, and a steady state (defined by a plateau) in the case of protein Arp2/3 added, while it is characterized by an increasing straight line if proteins are not added<sup>38</sup>. The data were finally collected and analyzed using the Software OriginLab.

Parameters	Settings
Measurement Mode	Kinetic
<ul style="list-style-type: none"> <li>• Time</li> <li>• Interval</li> <li>• Reads</li> </ul>	60:00 00:00:30 81
Absorbance Wavelength	310 nm
Plate Type	96 Well Standard clrbtm
Shaking before	5s Orbital, Medium
Shaking between	5s Orbital, Medium
Speed Read	On
Reading Order	Row
Designation of blank	First value automatically set to zero

Table 6. *Microplate reader parameters*

#### 4.2.4 KEITHLEY Measurement

The impedance of our samples was measured with the same device described in chapter 3.

The solutions were perfused into the experimental chamber of the parallel-plate contact device collected to the Keithley, using a micropipette tip at one opening, and a filter paper at the other opening for suction the excess. The frequency range of the measurement was set from 1 kHz to 10 MHz and data were subsequently collected. After each data collection and before the next one we washed the chamber with buffer, the General Actin Buffer. We also paid attention to any bubbles that could form in the chamber during the measurements, eliminating them and repeating the measurement, if necessary, in order to avoid any alterations in the results. The solution analyzed were solutions of actin filaments at 3 different concentrations, 0.9 mg/ml, 0.35 mg/ml and 0.1 mg/ml, solution with globular actin, not polymerized at 2 different concentrations, 0.35 mg/ml and 0.1 mg/ml and buffers such as General Actin Buffer (GAB) and GAB with ATP and DTT added.

## 4.3 Results

### 4.3.1 Turbidity Measurement

The biological activity of AKL99 is assessed by an actin polymerization assay. The ability of globular actin to polymerize into filament can be observed from the increase in optical density of actin solution at OD310nm (Figure 20).

Polymerizations were carried out as indicated in the Materials and Methods at 25°C with the SpectraMax® iD5 microplate reader. We analyzed 2 different concentrations of actin in our samples. As we can see from the figures, the polymerization in the case of 0.35 mg/ml is more evident and it has a linear trend, and it has been smoothed with a Fast Furier Transform of a 4 points window. In both cases we couldn't see the classical assembly in three steps, such as nucleation phase, elongation phase and steady-state phase, steps that are due to proteins concentration such as Arp2/3 or VCA, that weren't included in the experimental solutions.<sup>38</sup> Once the successful polymerization of actin filaments has been verified, we proceeded to study the impedance with the Keithley device.

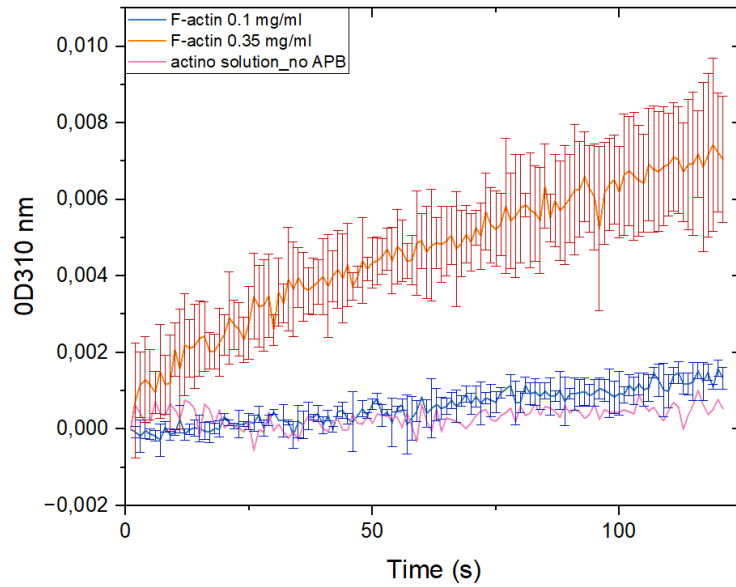


Figure 20 Standard polymerization reactions of samples of actin at different concentrations: 0.35 mg/ml and 0.1 mg/ml. A control solution without the addition of actin polymerization buffer has been analyzed as well.

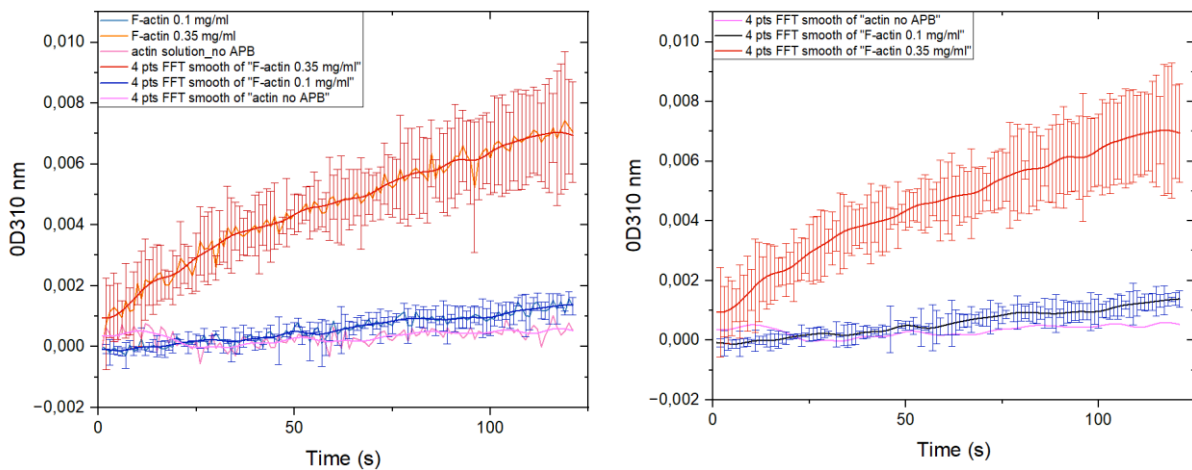


Figure 21 The data obtained have been smoothed with FFT windows of 4 points.

### 4.3.2 KEITHLEY

We obtained different curves that have been fitted using analysis tools in Origin. From Figure 22 and 23 we can observe the differences in impedance and in phase for the actin filaments, globular actin solutions and their background. In Figure 22a and Figure 23a all the samples are compared, while in 22b and 23b we can focus on F-actin and G-actin solutions at different concentrations. From these curves we can notice that G-actin has a similar trend to the buffers and has a higher impedance than the filaments. Moreover, we reported the module of the admittance in Siemens (Figure 24) to compare the conductance, and from that we can see that the actin filaments have higher conductance than the globular actin.

Successively we have subtracted the impedance and theta values of the media from the one of the solutions, to valuate better the differences (Figure 28). In the next paragraph we will use these data to model a circuit RLC and try to explain these trends. Afterwards, we divided the impedance in real and imaginary part. From the curves we can see in Figure 24b we can observe that the filaments that are formed have a very low impedance ( $\sim 10^2$ ) and it increases increasing the actin concentration. On the other hand, the solution of G-actin is 10 times above and it increases with the concentration as well. We can notice even a difference in the trend of the curves. G-actin solutions have a constant impedance until they the  $10^6$  frequency is reached, while the F-actin we can observe a first decreasing values of impedance at low frequencies to then maintain a constant value up to  $10^6$ , to then increase exponentially as the frequency go up. Even the behavior of the phase shows characteristic differences if we compare G-actin and F-actin solutions. In the case of the filaments, indeed, we have a peak in which the imaginary part arrives near to zero, at the frequency  $10^5$ , while a different trend characterizes the globular actin phase. A hypothesis to explain this behavior will be exposed in the next paragraph.

The curves obtained in Figures 28 and 29 represent the actin solution samples subtracting the values of the background. To do this subtraction we have considered the globular actin as in series to the elements of the media, while regarding the filaments, we have assumed them as in parallel with each other and with the media as well. Thus, different calculations were made to obtain the final graphs and more details will be reported in the next paragraph.

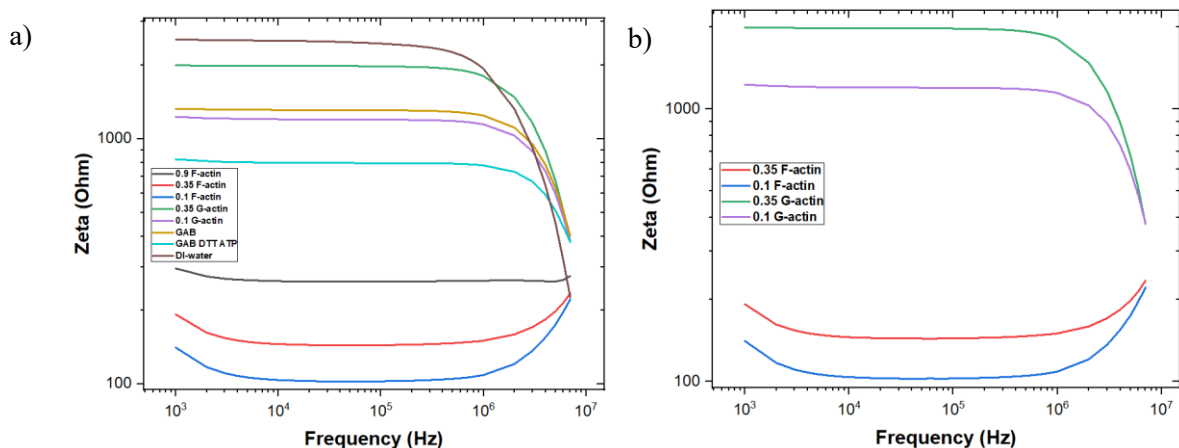


Figure 22. Impedance  $Z$  of the actin samples and buffers.

b)

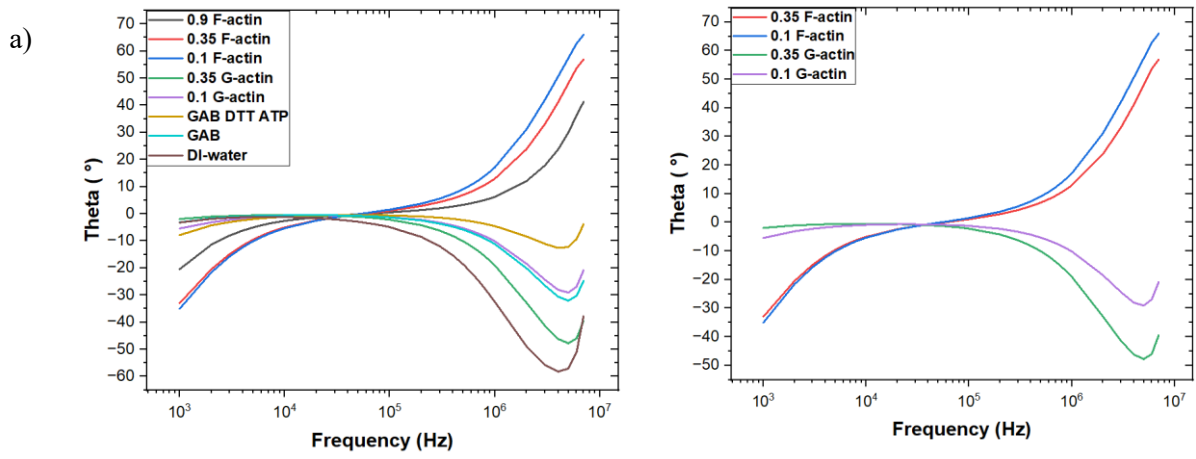


Figure 23. Phase in degrees of actin solutions and buffers.

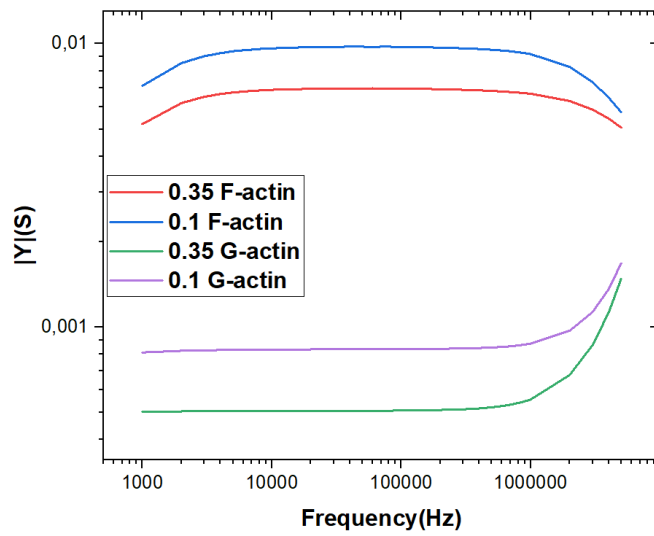


Figure 24. Module of the admittance of G-actin and F-actin solutions at different concentrations.

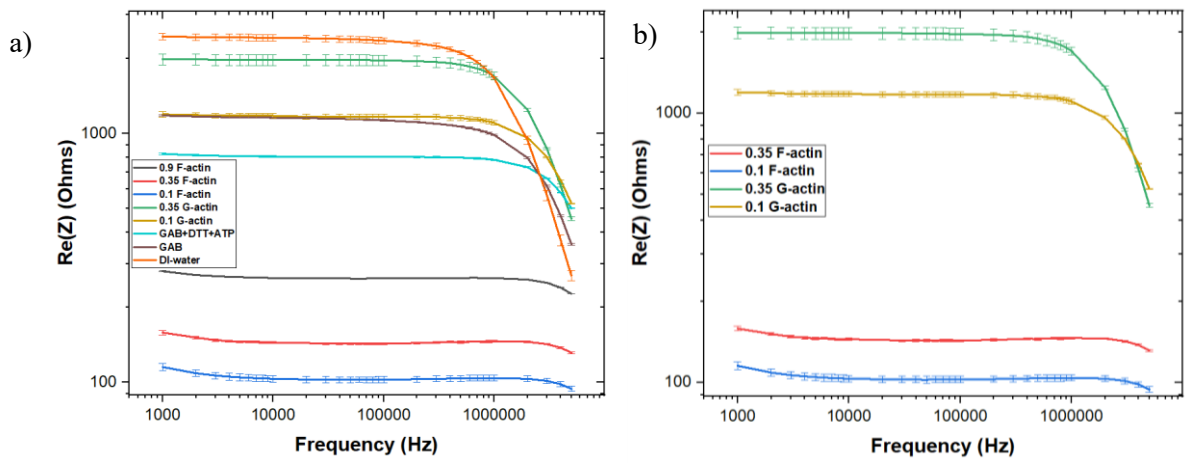


Figure 25. Real part of the impedance of G-actin, F-actin and buffer solutions. b) focus on G-actin and F-actin at different concentrations

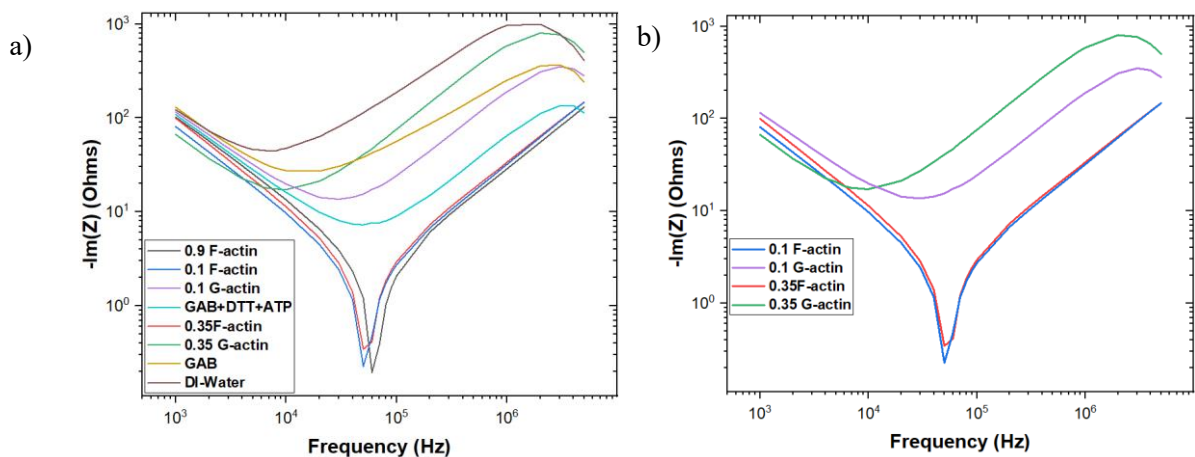


Figure 26. Imaginary part of the samples analyzed. b) focus on G-actin and F-actin solutions.

#### 4.3.3 Data Analysis

##### *Capacitive contributes in our solutions*

Starting from the results of our measurements, the conditions that allow actin filaments to operate as electrical transmission lines for ion fluxes along their lengths were explored. We propose a model in which each actin monomer is an electric element with capacitive, inductive, and resistive properties due to the actin filament's molecular structure and solution viscosity. The physical significance of each component for each section of the electrical network is described below.

According to Manning's theory,<sup>33</sup> as negatively charged polyelectrolytes, actin filaments may contain a proportion of their surrounding counterions in the form of a "condensed" cloud around their length and this is dependent in particular on the dielectric constant of the surrounding medium and on the ionic concentration of the solution. (Figure 27)

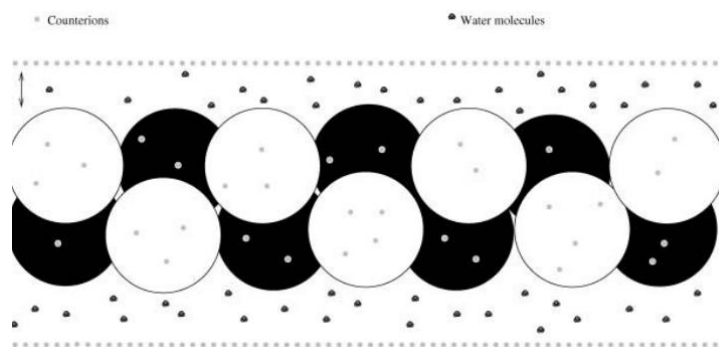


Figure 27. Positive counterionic charges in the bulk form a cylinder around the F-actin filament. There also are some counterions that condense to the actin filament.<sup>9</sup>

Further, whereas each of the units of globular actin, that give origin to the filaments, have tight bindings and form a double-stranded helix, the distribution of counterion clouds is nonuniform along the filament's length. Thus, it is similar to a solenoid with

fluctuating current flowing due to voltage differences generated by the ends of the filament. Additionally, this overcast of counterions provides F-actin with both resistive, capacitive and inductive behaviors that are associated with a highly conductive medium. The inductive component to the electrical properties of ionic waves is due to actin's double-stranded helical structure that induces the ionic flow in a solenoidal manner.

Ion flow is expected at a radial distance from the center of the filament, which is approximately equal to the Debye length and this distance depends on the ionic concentration of the medium.

We had 2 sample solutions with actin filaments in the media, at 2 different concentrations, 7  $\mu\text{M}$  and 2  $\mu\text{M}$ .

The filaments were assumed long  $\sim 1 \mu\text{m}$ , and, considering each monomer long 5 nm, we could calculate the number of actin monomers in 1 filament of the helix ( $N_1 \sim 200$ ) and the total number of actin monomers in double stranded filament ( $N_2 = 400$ ).

$$N_1 = \frac{1 \mu\text{m}}{5,5 \text{ nm}} = 181,8;$$

$$N_2 = 2 * 200 = 363$$

In the case of 7  $\mu\text{M}$  of actin concentration, considering the volume of the chamber of measurement as 2,625  $\mu\text{l}$ , the total number of actin monomers is considered around  $\sim 10,685 \times 10^{12}$ .

In conclusion the number of actin filaments in the chamber of the conductance measurements was  $\sim 2,197 \times 10^9$ .

$$N_{fil7} = \frac{10,685 * 10^{12}}{363} = 29,4 * 10^9$$

While in at 2  $\mu\text{M}$  of actin concentration, the total number of actin monomers in the chambre is around  $\sim 3,053 \times 10^{12}$  and the number of actin filaments in the chambre of the conductance measurements was  $\sim 8,41 \times 10^9$ .

$$N_{fil2} = \frac{3,053 * 10^{12}}{363} = 8,41 * 10^9$$

Our final idea was to find an accurate model constituted by capacitors, resistance and, in case, inductors, to explain the electrical behavior of our actin filaments in the media. From the curves previously reported we can see there is a big difference between the ones of the filaments and the others.

First of all, starting from our experimental graphs, we calculated the total resistance and capacitance of our system. The following formulas and tables report what we found in terms of capacitance and resistance. The capacitance has been calculated considering the lowest frequency available (1kHz).

$$Z = \sqrt{Re^2 + Im^2}$$

$$\tilde{R} = Re(Z)$$

$$\tilde{C} = \frac{1}{Im(Z) * w_i}$$

In Table 7 are reported the values of the total capacitance and resistance of the actin filaments in the media. As we can see, increasing the concentration of actin in solution,

the total capacitance decreases while the resistance increases. In Table 6 are reported capacitive and resistive contribution of solution with unpolymerized globular actin in solution and we can see a difference with the previous results since increasing the actin concentration in the media, the capacitance increases and the resistance decreases. In conclusion in Table 7 we reported the contribution in capacitance and resistance of the media itself, considering both, general actin buffer, and GAB with the addition of ATP and DTT.

<b>Actin Filament</b>	$\tilde{C}_f$ (F)	$\tilde{R}_f$ ( $\Omega$ )
<b>18 <math>\mu</math>M</b>	9,816 x 10 <sup>-6</sup>	279,55
<b>7 <math>\mu</math>M</b>	10,063 x 10 <sup>-6</sup>	158,411
<b>2 <math>\mu</math>M</b>	12,382 x 10 <sup>-6</sup>	115,21

Table 7. *Total capacitance and resistance contribution for solutions of actin filaments at different concentration in the media.*

<b>Globular actin</b>	$\tilde{C}_g$ (F)	$\tilde{R}_g$ ( $\Omega$ )
<b>7 <math>\mu</math>M</b>	14,998 x 10 <sup>-6</sup>	932,33
<b>2 <math>\mu</math>M</b>	8,663 x 10 <sup>-6</sup>	1194,435

Table 8. *Total capacitance and resistance contribution for solutions of unpolymerized globular actin at different concentration in the media.*

<b>Buffer</b>	$\tilde{C}_{\text{buffer}}$ (F)	$\tilde{R}_{\text{buffer}}$ ( $\Omega$ )
<b>GAB</b>	7,6896 x 10 <sup>-6</sup>	1181,364
<b>GAB+DTT+ATP</b>	9,2364 x 10 <sup>-6</sup>	827,951

Table 9. *Total capacitance and resistance contribution for solutions with just media.*

We then subtracted the influence of the media and calculated the electrical element characterizing each filament. We assumed that the impedance of each filament was in parallel with each other and with the media itself. Thus, the following formulas represent this calculation of the impedance and the relative real and imaginary part.

$$Z_f = \frac{1}{\frac{1}{Z_{f+m}} - \frac{1}{Z_m}} = \frac{1}{\frac{Z_m - Z_{f+m}}{Z_{f+m} * Z_m}} = \frac{Z_{f+m} * Z_m}{Z_m - Z_{f+m}}$$

$$\text{Re}(Z_f) = \frac{[(x^2 + y^2) * u + (u^2 + v^2) * x]}{(u^2 + v^2) - (x^2 + y^2)}$$

$$\text{Im}(Z_f) = \frac{[(x^2 + y^2) * v + (u^2 + v^2) * y]}{(u^2 + v^2) - (x^2 + y^2)}$$

con:

$$x = \text{Re}_{f+m};$$

$$y = \text{Im}_{f+m}$$

$$u = \text{Re}_m$$

$$v = \text{Im}_m$$

With the data found, calculated as described above, we got the curves of actin filaments that are showed in Figures 28, 29. On the other hand, as regards the solutions of unpolymerized globular actin, we assumed the globular elements as components in series with the media, so we simply subtracted the background data. The results are reported in comparison with actin filaments solution, and we reported the capacitance and impedance of them in Table 10 and 11.

<b>Actin Filament – Buffer (GAB+DTT+ATP)</b>	$\tilde{C}_f$ (F)	$\tilde{R}_f$ ( $\Omega$ )
<b>18 <math>\mu</math>M</b>	7,534 x 10 <sup>-6</sup>	441,596
<b>7 <math>\mu</math>M</b>	9,063 x 10 <sup>-6</sup>	210,494
<b>2 <math>\mu</math>M</b>	11,525 x 10 <sup>-6</sup>	142,77

Table 10. *Capacitive and resistive contribute of all the filaments, subtracting the buffer contribute.*

<b>Globular Actin – Buffer (GAB+DTT+ATP)</b>	$\tilde{C}_g$ (F)	$\tilde{R}_g$ ( $\Omega$ )
<b>7 <math>\mu</math>M</b>	24,04 x 10 <sup>-6</sup>	1169,275
<b>2 <math>\mu</math>M</b>	139,56 x 10 <sup>-6</sup>	366,019

Table 11. *Capacitive and resistive contribute of the globular actin, subtracting the buffer contribute.*

We now calculated the capacitive and resistive contribute of a single actin filament and of a single actin monomer comparing our results with theoretical calculations.

Considering the total number of actin filaments in the chamber of measurement as  $29,4 \times 10^9$ , as we mentioned previously in the paragraph, we obtained the capacitance of a single filament  $C_{fil7} = C_f / N_{fil7} = 0,324 \times 10^{-15}$  F and  $C_{fil2} = C_f / N_{fil2} = 1,370 \times 10^{-15}$  F, for the actin filament at concentration 7  $\mu$ M and 2  $\mu$ M respectively.

We extended our set of assumptions to calculate the resistance of a single actin filament 1  $\mu$ m long in a 7  $\mu$ M concentration solution. Here, the total resistance of the F-actin meshwork would be given by  $R_f$ , while each filament has resistance  $R_{fil7} = R_f / N_{fil7} = 7,16 \times 10^{-9}$   $\Omega$  and  $R_{fil2} = R_f / N_{fil2} = 16,97 \times 10^{-9}$   $\Omega$ .

To determine if these values were consistent with theoretical predictions which depends on the ionic concentration the total capacitance of a single filament has been calculated by previous models to be given by <sup>9</sup>:

$$C_{fil,teor} = \frac{2\pi\epsilon_0\epsilon l}{\ln\left(1 + \frac{\lambda_D}{r}\right)}$$

Where  $l$  is the length of the filament,  $\epsilon_r$  is the relative permittivity and  $\lambda_D$ , defined as Debye length, is given by

$$\lambda_D = \sqrt{(\epsilon_0\epsilon_r k_B T) / (2N_A c_s e^2)}$$

This length depends on the ionic concentration of the buffer, which in our case it is 500 mM. Thus, we are in physiological conditions, and the Debye length is approximatively 0.8 nm.<sup>15</sup>

Indeed, positive counterionic charges in the bulk are expected to form a cylinder at a radius greater than the actin filament itself, away from the actin surface, which includes the condensed ions.

$$r_{actin} < r < r_{actin} + \lambda_D$$

The permittivity,  $\epsilon$ , is given by  $\epsilon = \epsilon_0\epsilon_r$ , where  $\epsilon_r$  is the relative permittivity, which we should be in a range between  $3 < \epsilon_r < 10$ . We will assume  $\epsilon_r = 6$ . We take the length of an actin monomer typically as  $a = 5,5$  nm and the radius of the actin filament,  $r_{actin}$ , to be  $r_{actin} = 2,5$  nm (Chasan et al., 2002).

Finally, the capacitance  $C_0$  for a single actin monomer found by Cantiello et. Al. is found to be approximatively  $96 \times 10^{-6}$  pF.<sup>9</sup>

Substituting the length of our actin filament and considering  $r = 2,75$  nm we found that the theoretical capacitance for a single actin filament is  $C_{fil,teor} = 1,3 \times 10^{-15}$  F.

Thus, with these assumptions, our results are consistent with the theoretical capacitance in the case of 2  $\mu$ M concentration ( $1,37 \times 10^{-15}$  F), while in the case of 7  $\mu$ M of actin concentration in the solution, we have obtained a lower value ( $0,324 \times 10^{-15}$ ), precisely 4 times lower than the theoretical result.

$$C_{fil7} = \frac{C_{fil\_teor}}{4}; \quad C_{fil2} \approx C_{fil\_teor}$$

According to the paper just cited, although, regarding the sample of 7  $\mu$ M, we would have expected a higher value, this could be an effect due to a more complex organization of the filaments in the solution. Indeed, the concentration is higher, and the filaments could form also series connections between each other. Moreover, in the F-actin solution some globular actin could not have polymerize, contributing to the series connection.

Considering that we started from the assumption that the actin filaments are in parallel to each other, from the obtained result of capacitance of the filament, we can say that in the case of 7  $\mu$ M of actin concentration, only one out of 4 filaments is in

parallel, while the others can be considered in series.

Regarding the G-actin solution instead, we have considered the globular actin components in series with each other and the media.

The monomer of actin cannot be modeled with the previous theoretical capacitance since it is not comparable to a cylinder, but it has an almost spherical geometry.

The formula for the theoretical capacitance of a spherical capacitor is given by

$$C_{g,teor} = 4\pi\epsilon_0\epsilon_r \frac{r(r + \lambda_D)}{\lambda_D}$$

Where  $\lambda_D$  is the Debye length, given by the subtraction of the external ratio, corresponding to the max distance at which are the counterions, and the inner ratio, the one of the monomers itself.

We already said that the total number of actin monomers measured in the chamber was  $10,7 \times 10^{12}$  in the  $7 \mu\text{M}$  concentration solution and  $2,197 \times 10^9$  at  $2 \mu\text{M}$ , and that the ratio of a monomer is  $2,5 \text{ nm}$ . Considering  $\lambda_D = 0,8 \text{ nm}$ , and  $\epsilon_r = 6$ , for the same assumptions explained above, we find that the theoretical value for a single monomer of actin is  $C_{g,teor} = 6,88 \times 10^{-18}$ .

Dividing the total capacitance of G-actin solutions at the 2 different concentrations, obtained in our experiments, for the number of actin monomers present in each chamber, we obtained that in the first case the experimental capacity of a single monomer is equal to  $2,25 \times 10^{-18}$  ( $7 \mu\text{M}$ ) and in the second case is equal to  $6,35 \times 10^{-14}$  ( $2 \mu\text{M}$ ).

The first value obtained is really close to the theoretical result, while the second one it is probably due to an error during the measurement, as the obtained curve is also very different from the expectation.

#### *Inductive contributes in our solutions*

Another important aspect not analyzed yet is the inductive contribute of the actin filaments. Indeed, we suppose that this is due to actin's double-stranded helical structure that induces the ionic flow in a solenoidal manner.

In particular, it's known that the inductance doesn't contribute at low frequencies, while it does at high frequencies. Said that we calculated this feature at the correspondent frequency at which the imaginary part of Z tends to zero.

$$L = \frac{1}{C * \omega_0^2}$$

In Table 12 are reported the capacitive and inductive contributes of the solutions with actin filaments at different concentrations.

Actin Filament	$\tilde{C}_f(F)$	$L_f(H)$
<b>18 <math>\mu\text{M}</math></b>	$9,816 \times 10^{-6}$	$\approx 28,55 \times 10^{-6}$
<b>7 <math>\mu\text{M}</math></b>	$10,063 \times 10^{-6}$	$\approx 39,75 \times 10^{-6}$
<b>2 <math>\mu\text{M}</math></b>	$12,382 \times 10^{-6}$	$\approx 32,3 \times 10^{-6}$

Table 12. *Total capacitance and inductance contribution for solutions of actin filaments at different concentration in the media.*

In the first case the correspondent frequency, at which we find the peak,  $w_0$  was  $60 \times 10^3$ , in the second and third case  $50 \times 10^3$ .  
 In Table 13 instead, we report these contributions considering only the filaments, subtracting the data of the background as previously explained.

<b>Actin Filament – background (GAB+DTT+ATP)</b>	$\tilde{C}_g(F)$	$L_f(H)$
<b>18 <math>\mu</math>M</b>	$7,53 \times 10^{-6}$	$18,133 \times 10^{-6}$
<b>7 <math>\mu</math>M</b>	$9,063 \times 10^{-6}$	$27,7 \times 10^{-6}$
<b>2 <math>\mu</math>M</b>	$11,52 \times 10^{-6}$	$27,74 \times 10^{-6}$

Table 13. *Capacitance and resistance contribute due to only actin filaments at different concentrations.*

As we can see, the inductive and capacitive contributes have the same order in magnitude.

On the other hand, we also tried to calculate in the same way if also the globular actin could be modeled with an additive inductive component. In Table 14 we reported our calculations in the case of subtraction of the media's data.

<b>Globular Actin – Buffer (GAB+DTT+ATP)</b>	$\tilde{C}_g(F)$	$L_f(H)$
<b>7 <math>\mu</math>M</b>	$24,04 \times 10^{-6}$	$13,03 \times 10^{-9}$
<b>2 <math>\mu</math>M</b>	$139,56 \times 10^{-6}$	$51,33 \times 10^{-9}$

Table 14. *Capacitive and inductive contribute of the globular actin, subtracting the buffer.*

In this case we can see that the inductive contribute is 3 orders of magnitude lower than in the F-actin solutions. This confirm that the sinusoidal shape of the filaments and of these condensed clouds of counterions in their surroundings, contribute with giving an additional inductive behavior to these nanowires.

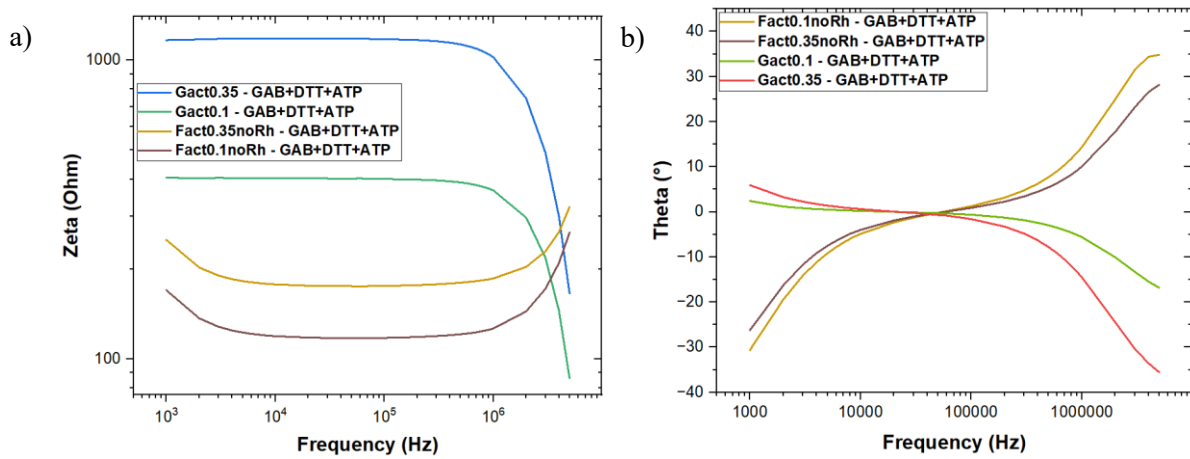


Figure 28. Subtraction of the background data from the sample's solutions.

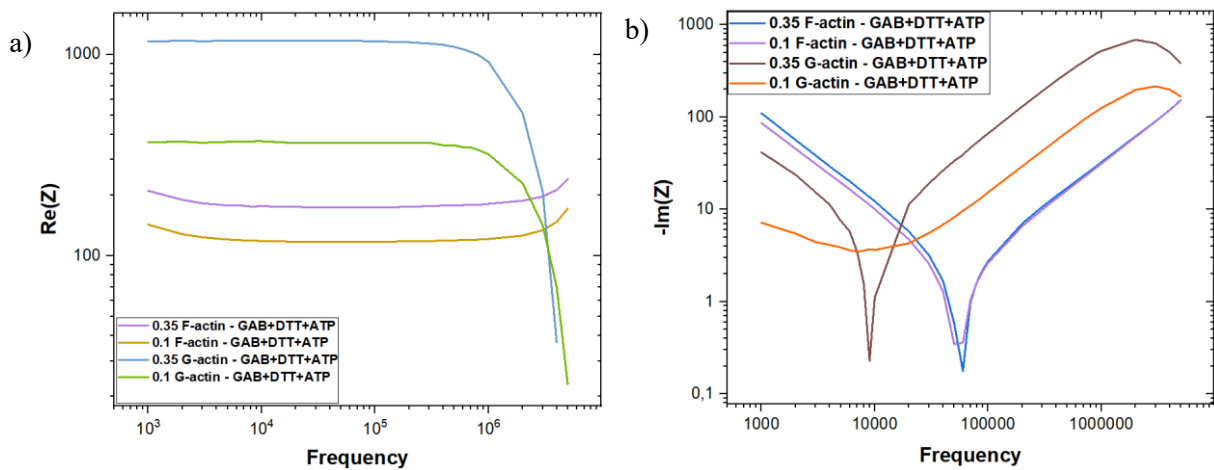


Figure 29. Subtraction of the background data from the sample's solutions a) Real part of impedance b) Imaginary part.

### Creation of a model

As we already have said, we have considered actin filaments in parallel with each other, and with the media as well. A possible scheme of the circuit is represented in Figure 30, where  $Z_0$  is the impedance of the external elements,  $Z_s$  the one of the solutions,  $R_h$  is the small constant resistance that represent the small fraction of unpolymerized globular actin and  $Z_{filn}$  the total impedance of each filament.

To give a further explanation to what is the meaning of our curves changing the frequencies, we hypothesized that depending on where we are on the frequency axis, we could fall into the condition of percolated resistors or percolated capacitors.<sup>25</sup>

In other researchers has been investigated the conduction flow-paths through disordered random composite media in terms of new medium approximation (MEMA) formula and RC networks and has been studied the frequency dependent admittance of large two-dimensional square resistor-capacitor networks. We observed in detailed our data for the module of admittance and for the phase and we noticed that the solutions of G-actin and of the buffers can be described as RC networks with

percolated resistors as we can find several similarities between the theoretical admittance and phase represented and our results. On the other hand, the actin filaments seem to have a different behavior. Looking at the phase the trend reminds a combination of a RC circuit characterize by percolated resistors at low frequencies, and percolated capacitors at high frequencies. While looking at the admittance, our experimental curves for actin filaments in solution we couldn't find any similarities. The reason may be related to the role of the inductive contribute that we found to exist in these solutions.

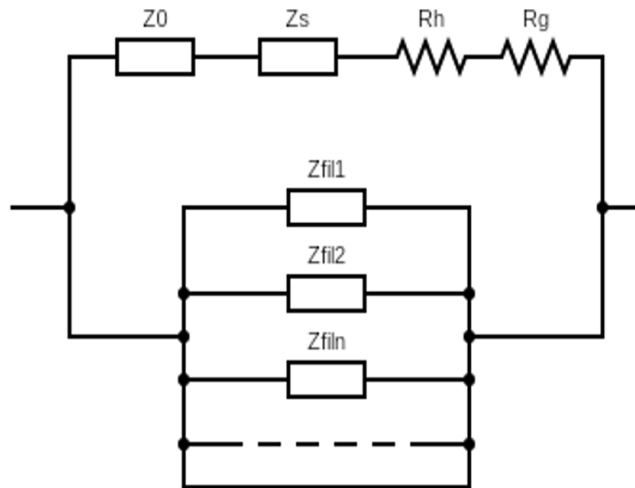


Figure 30. Model of filaments in parallel with the media.

# Chapter 5

## 5 Conclusions

First of all, the results in this work show the successful reconstitution and polymerization of our microtubules and actin filaments and subsequently it is shown how the gold nanoparticles actually managed to bind to microtubule biotemplates. Finally, we attempted to explain what we found with the impedance measurements by starting with the observation of how the medium around the samples affects the ion flux led by the microtubules and filaments, creating a condensed cloud of counterions around their length. Subsequently, based on these observations, we suggested a possible accurate model to explain our results and calculating the real and imaginary part and the admittance from the impedance measurements, we were able to extrapolate interesting features.

Regarding the gold nanoparticles functionalized microtubules in BRB80, we obtained linear results with other works, whereas regarding the samples in the diluted background, we would have expected the MTs to be clearly distinguished as highly conductive wires in a non-conductive medium. In our case, instead, despite expectations, we found that microtubules with gold nanoparticles increase the impedance of the media. Moreover, in both cases seems that the medium deeply influences the total conductivity, which confirms the formation of a condensed layer of ions in the surrounding.

In our model the MTs have been considered in parallel with each other and with the media, and knowing the total number of MTs present in the solution, we calculated the contribute of a single MT. In this way we found similar values of resistance for both the considered concentrations, but the MT in BRB80 resulted slightly more conductive, so this may confirm that the buffer still has an effect on the microtubules.

To summarize, the final results are almost linear with the predictions, and the ionic concentration of the buffer influences the capacitive contribute of a single MT with gold nanoparticles. Furthermore, we can assume that the gold nanoparticles on the microtubules have an effect on them, as the capacitive contribution in the presence of BRB80 is lower than the theoretical value, whereas it is four times higher in a diluted buffer. Furthermore, another hypothesis is that percolated resistor networks form in the considered RC circuit. Nonetheless, more research is required to better clarify these features and find the ideal model for this system.

As for the measurements on the actin filaments, the conditions that allow actin filaments to operate as electrical transmission lines for ion fluxes along their lengths were explored. We proposed a model in which each actin monomer is an electric element with capacitive, and resistive properties due to the actin filament's molecular structure and solution viscosity, and inductive behaviors associated with the actin's double-stranded helical structure that induces the ionic flow in a solenoidal manner.

Regarding the capacitive contribute for a single actin filament we found consistent results with the theoretical capacitance. Nevertheless, regarding the sample of 7  $\mu\text{M}$ , we would have expected a higher value, but this could be an effect due to a more complex organization of the filaments in the solution. Indeed, the concentration is higher, and the filaments could form also series connections between each other. Moreover, in the F-actin solution some globular actin could not have polymerize, contributing to the series connections.

Regarding the G-actin solution instead, considering the globular actin components as spherical element in series, and comparing their capacitive contribute to theoretical results, we found reasonable linear results.

We observed the admittance and phase curves of our sample's measurements, and we compared them with other researchers where it was investigated the conduction flow-paths through disordered random composite media and frequency dependent admittance of large two-dimensional square RC networks. We discovered that the G-actin and buffer solutions can be described as RC networks with percolated resistors by observing several similarities between the theoretical admittance and phase represented and our results. Actin filaments, on the other hand, appear to behave differently. When viewed in phase, the trend resembles a combination of an RC circuit with percolated resistors at low frequencies and percolated capacitors at high frequencies but couldn't find any similarities between our experimental curves for actin filaments in solution and the admittance curves. The reason could be related to the role of the inductive contribution and moreover, increasing the concentration of proteins in solution, may cause percolated behavior, and R, L and C elements start forming networks between each other.

## **5.1 Future perspectives**

The entire study has led to results that deserve further study and an analysis that explains and confirms the values previously obtained and the hypothesized characteristics. For example, it would be interesting to compare the behavior of bare microtubules with those coated with gold nanoparticles to better understand the differences and the role of the nanoparticles. Another analysis that could be carried out is the development and improvement of an electric model for G-actin and F-actin. Some results seemed not clear, so it might be best to try them again for more consistent results.

# Bibliography

1. Wade, R. H. On and around microtubules: an overview. *Mol. Biotechnol.* **43**, 177–191 (2009).
2. Aeluri, M. *et al.* Small molecule modulators of protein-protein interactions: selected case studies. *Chem. Rev.* **114**, 4640–4694 (2014).
3. Hawkins, T., Mirigian, M., Yasar, M. S. & Ross, J. L. Mechanics of microtubules. *J. Biomech.* **43**, 23–30 (2010).
4. Kalra, A. *et al.* On the capacitive properties of individual microtubules and their meshworks. (2019).
5. Behrens, S., Habicht, W., Wu, J. & Unger, E. Tubulin assemblies as biomolecular templates for nanostructure synthesis: from nanoparticle arrays to nanowires. *Surf. Interface Anal.* **38**, 1014–1018 (2006).
6. Uzman, A. *Molecular Cell Biology* (4th edition): Harvey Lodish, Arnold Berk, S. Lawrence Zipursky, Paul Matsudaira, David Baltimore and James Darnell; Freeman & Co., New York, NY, 2000, 1084 pp., list price \$102.25, ISBN 0-7167-3136-3. *Biochem. Mol. Biol. Educ.* **29**, 126–128 (2001).
7. Dominguez, R. & Holmes, K. C. Actin structure and function. *Annu. Rev. Biophys.* **40**, 169–186 (2011).
8. Lin, E. C. & Cantiello, H. F. A novel method to study the electrodynamic behavior of actin filaments. Evidence for cable-like properties of actin. *Biophys. J.* **65**, 1371–1378 (1993).

9. Tuszyński, J. A., Portet, S., Dixon, J. M., Luxford, C. & Cantiello, H. F. Ionic wave propagation along actin filaments. *Biophys. J.* **86**, 1890–1903 (2004).
10. Hunley, C., Uribe, D. & Marucho, M. A multi-scale approach to describe electrical impulses propagating along actin filaments in both intracellular and in vitro conditions. *RSC Adv* **8**, 12017–12028 (2018).
11. Manrique-Bedoya, S. & Marucho, M. Molecular structure study on the polyelectrolyte properties of actin filaments. *RSC Adv* **12**, 6314–6327 (2022).
12. Kalra, A. P. *et al.* All Wired Up: An Exploration of the Electrical Properties of Microtubules and Tubulin. *ACS Nano* **14**, 16301–16320 (2020).
13. Inc. Cytoskeleton, “Tubulin Polymerization Assay Kit.” <https://www.cytoskeleton.com/pdf-storage/datasheets/bk006p.pdf>.
14. Mirigian, M., Mukherjee, K., Bane, S. L. & Sackett, D. L. Measurement of in vitro microtubule polymerization by turbidity and fluorescence. *Methods Cell Biol.* **115**, 215–229 (2013).
15. Eakins, B. B. *et al.* Modeling Microtubule Counterion Distributions and Conductivity Using the Poisson-Boltzmann Equation. *Front. Mol. Biosci.* **8**, (2021).
16. Santelices, I. B. *et al.* Response to Alternating Electric Fields of Tubulin Dimers and Microtubule Ensembles in Electrolytic Solutions. *Sci. Rep.* **7**, 9594 (2017).
17. Kalra, A. P. *et al.* Investigation of the Electrical Properties of Microtubule Ensembles under Cell-Like Conditions. *Nanomater. Basel Switz.* **10**, (2020).
18. Behrens, S., Wu, J., Habicht, W. & Unger, E. Silver Nanoparticle and Nanowire Formation by Microtubule Templates. *Chem. Mater.* **16**, 3085–3090 (2004).

19. Zhou, J. C. *et al.* Characterization of gold nanoparticle binding to microtubule filaments. *Mater. Sci. Eng. C* **30**, 20–26 (2010).
20. Long, D. A. Handbook of vibrational spectroscopy, volumes 1–5. Edited by J. M. Chalmers and P. R. Griffiths. John Wiley & Sons, Chichester, 2002, pp. 3862. *J. Raman Spectrosc.* **36**, 271–271 (2005).
21. Zhou, J. C. *et al.* Microtubule-based gold nanowires and nanowire arrays. *Small Weinh. Bergstr. Ger.* **4**, 1507–1515 (2008).
22. Pal, A. Photoinitiated gold sol generation in aqueous Triton X-100 and its analytical application for spectrophotometric determination of gold. *Talanta* **46**, 583–587 (1998).
23. Satarić, M. V., Ilić, D. I., Ralević, N. & Tuszynski, J. A. A nonlinear model of ionic wave propagation along microtubules. *Eur. Biophys. J.* **38**, 637–647 (2009).
24. Lamm, G. & Pack, G. R. Calculation of Dielectric Constants near Polyelectrolytes in Solution. *J. Phys. Chem. B* **101**, 959–965 (1997).
25. Aouaichia, M. *et al.* Understanding the anomalous frequency responses of composite materials using very large random resistor-capacitor networks. *Eur. Phys. J. B* **90**, 39 (2017).
26. Straub, F. B. in *Studies Int med Chem Univ Szeged* (ed Szent-Györgyi), 2, 3–15 (Karger, 1942).
27. Oda, T., Iwasa, M., Aihara, T., Maéda, Y. & Narita, A. The nature of the globular- to fibrous-actin transition. *Nature* **457**, 441–445 (2009).
28. Kabsch, W., Mannherz, H. G. & Suck, D. Three-dimensional structure of the complex of actin and DNase I at 4.5 Å resolution. *EMBO J.* **4**, 2113–2118 (1985).
29. Lodish, H. F. *Molecular cell biology. Molecular cell biology* (W.H. Freeman-Macmillan Learning, 2016).

30. Carrier, M. F. Actin: protein structure and filament dynamics. *J. Biol. Chem.* **266**, 1–4 (1991).
31. Alberts B, Johnson A, Lewis J, et al. *Molecular Biology of the Cell*. 4th edition. New York: Garland Science; 2002. Chapter 16, The Cytoskeleton. Available from: <https://www.ncbi.nlm.nih.gov/books/NBK21051/>. in.
32. Cantiello, H. F., Patenaude, C. & Zaner, K. Osmotically induced electrical signals from actin filaments. *Biophys. J.* **59**, 1284–1289 (1991).
33. Manning, G. S. The molecular theory of polyelectrolyte solutions with applications to the electrostatic properties of polynucleotides. *Q. Rev. Biophys.* **11**, 179–246 (1978).
34. Inc. Cytoskeleton, “Actin Protein (>99% Pure): Rabbit Skeletal Muscle” <https://www.cytoskeleton.com/actin/akl99> (accessed Nov. 10, 2022).
35. Doolittle, L. K., Rosen, M. K. & Padrick, S. B. Measurement and analysis of in vitro actin polymerization. *Methods Mol. Biol. Clifton NJ* **1046**, 273–293 (2013).
36. Cooper, J. A., Walker, S. B. & Pollard, T. D. Pyrene actin: documentation of the validity of a sensitive assay for actin polymerization. *J. Muscle Res. Cell Motil.* **4**, 253–262 (1983).
37. Laurent, V. *et al.* Role of proteins of the Ena/VASP family in actin-based motility of *Listeria monocytogenes*. *J. Cell Biol.* **144**, 1245–1258 (1999).
38. Inc. Cytoskeleton, “Arp2/3 Protein Complex” <https://www.cytoskeleton.com/pdf-storage/datasheets/rp01p.pdf> (accessed Nov. 10, 2022).